AMERICAN UNIVERSITY OF BEIRUT

MODELING DISLOCATION INTERACTION WITH GRAIN BOUNDARIES IN MARTENSITIC STEEL

by
OSSAMA JIHAD ABOU ALI MODAD

A thesis
submitted in partial fulfillment of the requirements
for the degree of Master of Engineering
to the Department of Mechanical Engineering
of the Maroun Semaan Faculty of Engineering and Architecture
at the American University of Beirut

Beirut, Lebanon
December 2021

AMERICAN UNIVERSITY OF BEIRUT

MODELING DISLOCATION INTERACTION WITH GRAIN BOUNDARIES IN MARTENSITIC STEEL

by
OSSAMA JIHAD ABOU ALI MODAD

Approved by:

[Signature]

Dr. Mu'tasem Shehadeh, Associate Professor — Advisor
Mechanical Engineering

[Signature]

Dr. Ramsey Hamade, Professor — Member of Committee
Mechanical Engineering

[Signature]

Dr. Mohammad Ahmad, Professor — Member of Committee
Chemical Engineering

Mohammad Ahmad

Date of thesis defense: December 16, 2021

AMERICAN UNIVERSITY OF BEIRUT

THESIS RELEASE FORM

Student Name: Abou Ali Modad ________Ossama ____________ Jihad_________
Last First Middle

I authorize the American University of Beirut, to: (a) reproduce hard or electronic copies of my thesis; (b) include such copies in the archives and digital repositories of the University; and (c) make freely available such copies to third parties for research or educational purposes:

☒ As of the date of submission

☐ One year from the date of submission of my thesis.

☐ Two years from the date of submission of my thesis.

☐ Three years from the date of submission of my thesis.

Ossama Modad____

Signature Ossama Modad Date January 10th, 2022

ACKNOWLEDGEMENTS

Firstly, I would like to express my sincere gratitude to my supervisor Dr. Mutasem Shehadeh for guiding me throughout this project. His insight and knowledge about dislocation dynamics has helped me better understand my findings and establish a researcher's mentality. His help in this project was invaluable and words cannot express my gratitude. Secondly, I wish to thank my committee members Dr. Ramsey Hamade and Dr. Mohammad Ahmad for being part of the thesis committee.

I wish to thank my friends Abdul Rahman El Bsat, Nabil Berjaoui, Ahmad Mahmassani and Dr. Pascale El Ters who were there for me whenever I needed to vent my frustrations.

My sincerest appreciation, respect and love go to my family for believing in me and for their unconditional support during these tough times, especially my brother, future Doctor, Bassel Modad. Thank you, Mom, Dad, and my dearest brother.

ABSTRACT
OF THE THESIS OF

Ossama Jihad Abou Ali Modad for Master of Engineering
Major: Mechanical Engineering

Title: Modeling Dislocation Interaction with Grain Boundaries in Martensitic Steel

Martensitic steels are widely used as a structural material in critical components found fossil fuel and nuclear power plants, such as boilers, pipes, and fittings. Martensitic steels are known to have a hierarchical microstructure that follows the Kurdjumov – Sachs (K – S) orientation relationship, where a prior austenite grain is composed of packets separated by high angle grain boundaries or packet boundaries, which are in turn divided into blocks or variants segregated by high angle grain boundaries called block boundaries. Blocks themselves are an agglomeration of laths divided by low angle grain boundaries named lath boundaries which have precipitates scattered on them. This work seeks to examine, using a couple dislocation dynamics – continuum mechanics approach called Multiscale Dislocation Dynamics Plasticity (MDDP), the interactions between dislocations and packet, block, lath boundaries and precipitates under uniaxial tension loading and their effect on the mechanical response of the material. The simulations are conducted at a strain rate of 10^5 s^{-1} at room temperature. The main crystallographic features that arise during the deformation process were extracted and analyzed in terms of their contribution to the mechanical response of the material. The orientation relationship governing the microstructure of martensitic steels, namely the K – S orientation relationship was incorporated in MDDP in an effort to accurately capture the deformation behavior of the material in question. The strength of lath martensitic steel was analyzed as a function of the lath width, block size, and packet size to determine the appropriate effective grain size.

TABLE OF CONTENTS

ILLUSTRATIONS

Figure

TABLES

Table

CHAPTER I

INTRODUCTION

A. Thesis Objective

The key aims of this work are to:

- Develop a three-dimensional model for accurate representation of a sample of lath martensitic steel.
- Develop a methodology to study the microstructural evolution of P91 steel under uniaxial tension.
- Study the microstructural interactions of dislocations with grain boundaries in P91 steel under static conditions.
- Study the size effect of different hierarchies in martensitic steel.

B. Thesis Significance

The usage of energy has improved the quality of life for humanity and resulted in major scientific and technological advancements. In the last three decades, global energy consumption increased by about two times, with the main energy source being fossil fuels. Worldwide electricity consumption is expected to increase three times over the next couple of decades. Fossil fuels, however, do not come without a drawback. To that end, countries that have agreed to the Kyoto Protocol and the Paris Agreement, commit to reduce their carbon dioxide emissions, and reduce their carbon footprint. In order to meet this objective, the countries under these agreements have taken to encourage and develop, financially and otherwise, renewable energy sources, especially wind power. Around 75% of the worldwide wind power is installed in Europe.

However, renewable energy is not without its own drawbacks. One major concern for power plant operators is consistency of supply. Integrating wind energy into the grid favors constraining wind power output to make sure that the load gradient that must be added by fossil fuel power plants is within their output capabilities so as to minimize the risk of plant damage due to the fluctuations in wind energy output (Protocol & Union, 1990). **Fig. 1** represents the fluctuating nature of wind power over a 24 hour period. This highlights the inadequate interfacing between wind power and the regular power grid which results in loss of wind power output. This drop in power output must be complemented by fossil fuel power. Even small fluctuations in wind speed will require the fossil fuel power plant to respond in a manner to supplement this shortcoming in wind power.

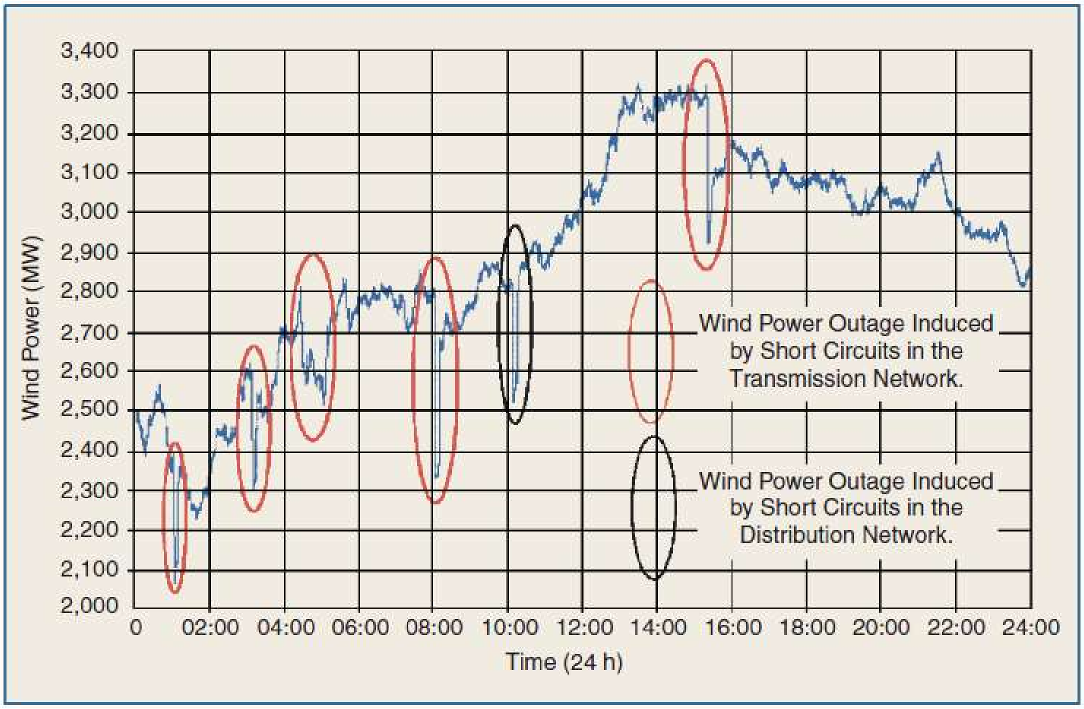

Figure 1. Wind power dips (Protocol & Union, 1990).

It is therefore expected that the frequency of plant start – ups and shut – downs will increase and will occur in an unpredictable fashion. The consequences of the increased number of start – ups imposes a risk on the plant life cycle and must be properly assessed and considered. To compensate for these frequent shutdowns, the efficiency of the electrical power plants must be increased. This also incentivizes the use of nuclear power plants and for fossil fuel power plants to increase their operating temperatures. For that purpose, proper structural materials must be developed to withstand the frequent shut – downs that lead to fatigue loading of power plant components. Failure of power plant components can occur suddenly and drastically.

This requires a thorough understanding of component failure and structural material performance.

C. Thesis Organization

Chapter II presents a literature review in terms of phenomenological and physical behavior of P91 steel and martensitic steels in general at macroscopic and microscopic levels. The different crystallographic orientation relationships in martensitic steels are reviewed. Grain boundaries and their role in material strengthening is examined, attention is given to their role in polycrystalline materials and the Hall-Petch relationship is related to grain boundaries. Computational and experimental analysis of P91 steel and power plant components are reviewed in order to establish the current state of the literature.

Chapter III describes the methodology used in this work and the simulation set – up. This chapter also describes how the low angle boundary is constructed and the implementation of the Kurdjumow – Sachs crystallographic orientation relationship in martensitic steel.

Chapter IV details the results obtained from the simulations of the lath boundaries which are then thoroughly discussed,

Chapter V presents the findings of the simulations where the K – S crystallographic orientation relationship is implemented to model the martensitic microstructure.

Chapter VI serves as a conclusion and summarizes the main findings of this study.

CHAPTER II

LITERATURE REVIEW

A. Introduction

Worldwide demand for energy efficiency incentivizes nuclear power plants and fossil fuel plants to increases their operating temperature. As such, structural materials with sufficient strength under the operating conditions must be developed. The prime candidate material for such applications is 9Cr martensitic steel, possessing high thermal conductivity, low thermal expansion coefficient and excellent resistance to irradiation(Wang et al., 2014). Commercial 9Cr steels such as P91 steels (i.e. 9Cr – 1Mo) can be used up to 590 and 620°C respectively(Zinkle & Busby, 2009). Microscopically, Grade 91 steels have a martensitic lath structure. High dislocation densities as well as precipitate strengthening are believed to be responsible for these materials' excellent high temperature strength. These steels play a crucial role in the power generation industry, as they act as the materials of essential power plants components (valve chambers, turbine cylinders, T-pipes, etc.) The constant start-ups and shut-downs during operation occur as a consequence of temperature gradients and thermal stresses. Repeated thermal stresses can lead to low cycle fatigue (LCF) damage in power plant components (Golański & Mroziński, 2013). LCF, according to (R.Viswanathan, 1989), is responsible of 65% of damages in turbine cylinders and valve chambers. Failure of power plant components is costly in terms of plant down time and maintenance costs. Thus, the need for predictive techniques, be they experimental or computational, to a comprehensive understanding of material behavior, therefore allowing for scheduled maintenance, inspection, and repair for vulnerable components.

B. Microstructure of Martensitic Steels

Modified 9Cr – 1Mo ferritic steel (alloyed with niobium and vanadium), also called P91 steels is widely used as a structural material at high temperatures in fossil fuel and modern nuclear power plants. 9Cr – 1Mo steels have seen major use in the tubing of reheater and superheater portions of said power plants(Nagesha et al., 2002). In order to be able to use these steels, they first must undergo the proper manufacturing and fabrication processes so as to obtain the desired microstructure and optimal mechanical properties for performing in a power plant environment. The microstructure of P91 steels is typically martensitic**.** This microstructure forms due to a heat treatment process. The material is first normalized for 2 h at temperatures of approximately 1100 °C, which results in an austenite structure. The material is then quenched in order to produce a martensitic transformation characterized by the lath martensite structure and high dislocation density. The next step is to subject the material to a tempering process at about 750 °C for 1 – 2h to improve ductility. Tempering results in the partial reduction of dislocation density and the formation of various precipitates(Barrett et al., 2014). Martensite, which has a BCC structure, is formed in low carbon steels when the austenite phase that has an FCC structure is quenched rapidly to a low temperature. The transformation from austenite to martensite is called the martensitic transformation. This transformation leads to a hierarchical structure characterized by a high initial dislocation density ($10^{13} – 10^{14}$ m^{-2}). When the austenite (γ) phase with a face – centered cubic (FCC) crystal structure in steels is rapidly quenched to a low temperature, a diffusionless transformation forms a new phase with body – centered cubic (BCC) crystal structure. The transformation and the resulting phase are called the martensitic transformation and martensite (α), respectively. The morphology and crystallographic orientation relationship between prior austenite grains and the transformed martensite blocks depend on alloy composition. Lath martensite forms in low carbon steels with a carbon content less than 0.6% with habit planes close to $\{111\}_{\gamma}$. The resulting structure is a three level hierarchy shown in **Fig. 3.** The largest substructure is called a 'packet' whose size can range from 15 to 500 µm. A packet is formed of grains called 'blocks' usually between 1 and 10 µm in size. The 'blocks' are in turn partitioned into 'laths' whose size ranges between 0.2 and 1 µm in width. It must be noted, however, that depending on the process and carbon content, the size of each hierarchy varies, and the range of values mentioned corresponds to a range of martensitic steels. Precipitates and dislocations, which are a key feature of the lath substructure are present within laths and on its boundaries. These precipitates are mainly present on the lath boundaries and between them. The most common precipitates found in martensitic steels are $M_{23}C_6$ carbides (M = Cr, Fe, Mo) contribute to the strength and toughness of the material by retarding sub – grain growth during the tempering process (Meade et al., 2018). Precipitates contribute to the higher performance of martensitic steels at higher temperatures by hindering dislocation motion during plastic deformation (Brian J. Golden et al., 2016). The mean diameter of precipitates is in the order of 10 – 600 nm. The boundaries between the lath, blocks and packets have been identified to be high angle grain boundaries (HAGBs) (Kitahara et al., 2006), while between laths, the boundaries were established as low angle grain boundaries (LAGBs). Typical chemical composition of P91 steel is shown in **Table 1.**

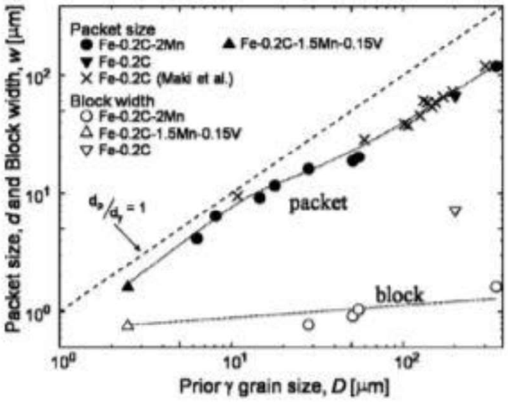

c

Figure 2. Packet size and block width variation with prior austenite (γ) grain size in various low carbon (0.2% C) alloys (Furuhara et al., 2008).

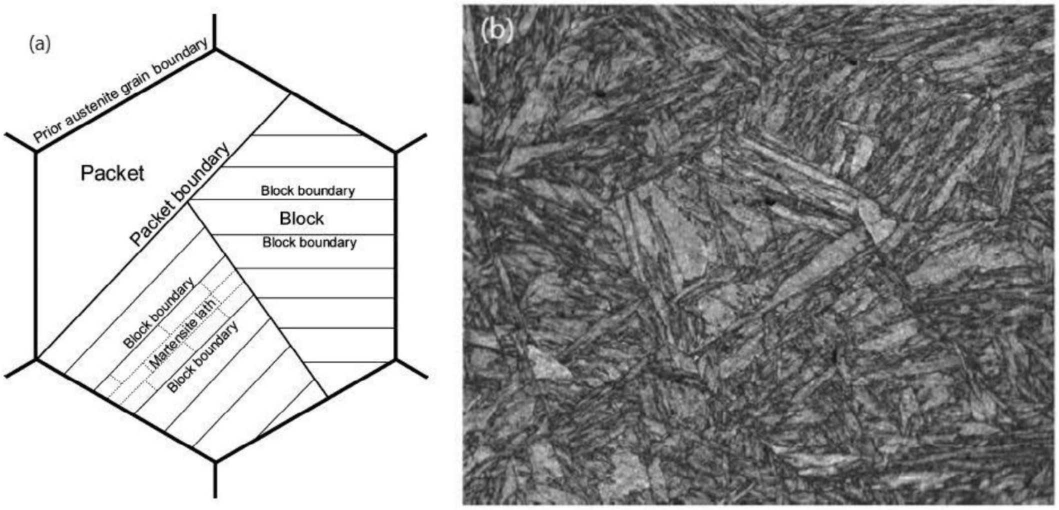

Figure 3. Hierarchical microstructure of martensitic steel (a) Schematic diagram of P91 microstructure (b) Image quality map obtained from SEM (Kitahara et al., 2006).

Table 1. Chemical composition of P91 steel(Pandey et al., 2016)

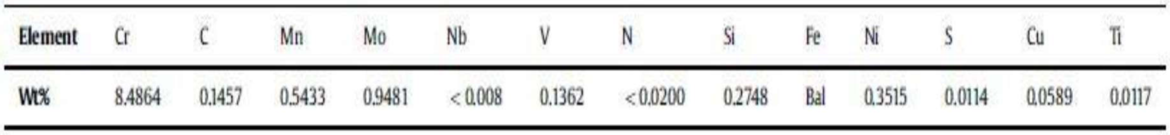

Element	Cr	C	Mn	Mo	Nb	V	N	Si	Fe	Ni	S	Cu	Ti
Wt%	8.4864	0.1457	0.5433	0.9481	< 0.008	0.1362	< 0.0200	0.2748	Bal	0.3515	0.0114	0.0589	0.0117

The packet and block morphologies change slowly with carbon content as shown in **Fig. 4.** (MAKI et al., 1980). As the carbon content increases up to 0.8%, the packets and blocks become finer and harder to identify in an optical micrograph. Small amounts of lenticular martensite forms in addition to lath martensite in the case of 0.8% carbon content. As stated previously, lath martensite forms in low carbon steels with a carbon content less than 0.6% with habit planes close to $\{111\}_\gamma$ (Morito et al., 2003). A number of lath martensite steels have been reported to follow the Kurdjumow – Sachs (K – S) orientation relationship (Kurdjumow & Sachs, 1930). It has been shown that Ni also affects the martensite morphology where Fe – 28.5%Ni steel forms plate martensite and has been shown to satisfy the Nishiyama – Wassermann (N – W) orientation relationship (Kitahara et al., 2005). The Kurdjumow – Sachs crystallographic orientation relationship will be discussed in detail in **Chapter 3**

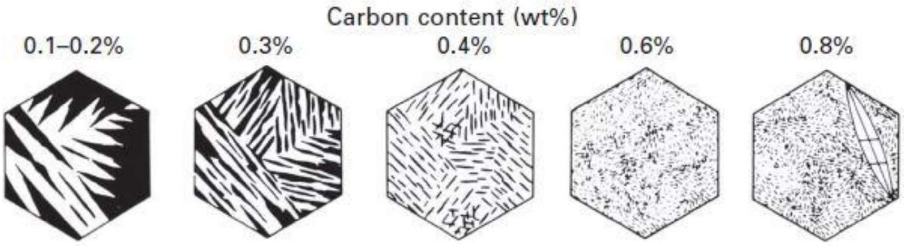

Figure 4. Schematic showing the morphology change at the optical microscope scale of lath martensite with carbon content in ferrous alloys (MAKI et al., 1980).

C. Grain Boundaries

Since HAGBs and LAGBs separate the different packets (and blocks) and laths respectively, the role of a grain boundary in material strengthening and its influence on material response under a certain loading condition must be thoroughly examined.

A grain boundary (GB) is an interface separating two grains, called crystallites, having different crystallographic orientations in a polycrystalline material. Grain boundaries are 2D interfacial defects. When the orientation mismatch between adjacent grains is slight, that is on the order of a few degrees (approximately 5° and up to 15°), then the boundary is called a low (or small) angle grain boundary.

The angle θ is related to the magnitude of the Burgers vector |b| and the separation distance between the dislocations d using Frank's formula:

$$\theta = \frac{|b|}{d} \qquad (1)$$

An LAGB is formed when edge dislocations are aligned in the manner of **Fig. 5.** The type of boundary shown below**.** is called a tilt boundary. A twist boundary is formed by an array of screw dislocations (Callister, 1991).

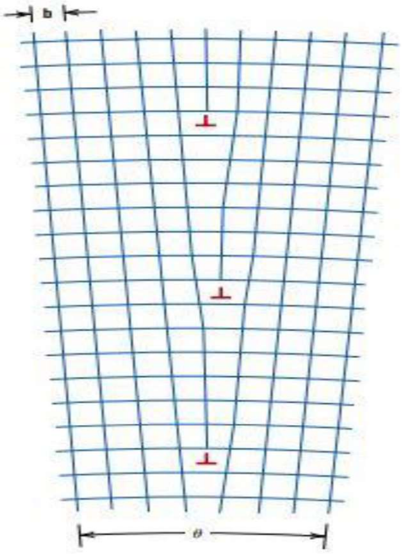

Figure 5. Schematic of an array of edge dislocations from a tilt boundary between 2 grains with misorientation angle θ (Callister, 1991).

The other type of GB is the high angle grain boundary (HAGB) where the misorientation angle between grains is larger than about 15°(Callister, 1991).

When a metal consists of a single crystal, dislocation glide is the main mechanism responsible for plastic deformation. However, for polycrystalline materials which consists of several grains with different orientations, plastic deformation is affected not only by dislocation glide but also by plastic flow across several grain boundaries (Sutton et al., 1996). Each grain has its own principal slip planes, or slip directions oriented differently from its neighbor's. Upon deformation, slip bands are observed in each individual grain. Figure 3 is a representation of a polycrystalline material as seen under a microscope, before and after deformation. The schematic assumes that the grains retain their shape and size after deformation, something which may occur only when the macroscopic deformation is very small. In polycrystalline materials, slip planes and slip directions vary from one crystal to another, which means that the critical resolved shear stress (CRSS) varies from one grain to the next. It thus follows that the crystal with the largest CRSS yields first followed by the one with the second largest CRSS and so on. If a grain is oriented unfavorably with respect to the direction of the applied stress, then the deformation is impeded. Yield criteria in polycrystalline materials is a balance between the slip mechanisms of each grain which are controlled by the CRSS. It is worth noting that polycrystalline materials undergoing microplastic deformation will not have all of its grains deformed plastically, that is either because the undeformed grains are not favorably oriented with respect to the applied load or the CRSS has not yet been reached in some crystals(Kondo et al., 2016).

The most notable explanation of plastic deformation in polycrystalline materials is the Hall-Petch relationship which accounts for the effect of grain boundaries on mechanical properties as shown in Equations (2) & (3).

$$\sigma_y = \sigma_0 + k_1 D_{GB}^{-1/2} \tag{2}$$

$$\sigma(\varepsilon) = \sigma_0(\varepsilon) + k_1(\varepsilon) D_{GB}^{-1/2} \tag{3}$$

Where σ_0, k_1, $\sigma_0(\varepsilon)$, $k_1(\varepsilon)$ are constants and D_{GB} is the grain size. Equations (1) and (2) are separated into two parts. The first part is independent of the grain size and the other part which is dependent on the grain size. In equation (2) for example, $\sigma_0(\varepsilon)$ is the flow stress of the grain interior and $k_1(\varepsilon)D_{GB}^{-1/2}$ is the contribution to the flow stress $\sigma(\varepsilon)$ due to the presence of grain boundaries. The Hall-Petch slope has been derived based on the dislocation pileup model against the boundary therefore hindering slip propagation(Pelleg, 2013).

The role of GBs in material strengthening is examined by studying the interaction between dislocations and GBs through TEM investigations and simulations. These studies highlight the effect of the GB structure and the character of dislocations interacting with the GBs. A study as early as 1988 has examined these interactions using static TEM experiments. It was found that GBs allow slip propagation from one grain to another by way of three modes: (1) Dislocation absorption into the GB, absorption and emission, and absorption – emission – reflection. Stress levels needed for dislocation transmission through the GB have been calculated for a set of GBs and were found to be higher than the macroscopic yield stress. Furthermore, the stress values calculated for the set of GBs varied widely, meaning that the GB contribution to material strengthening is the average of the strength of individual barriers. TEM experiments also showed that the most frequently observed mode of dislocation transmission is the absorption – emission – reflection mechanism(Hansen, 2005). A schematic of the dislocation – GB interaction is shown in **Fig. 6.** Grain 1 contains the incoming slip system, while grain 2 contains the outgoing slip system. Considering the geometry and Burgers vector of the incoming and outgoing dislocations, and in particular the residual Burgers vector of the dislocation left at the GB, various possible reactions can take place(Shen et al., 1988): (1) transmission via cross – slip, $\overrightarrow{b_1}$ and $\overrightarrow{b_2}$ are parallel to the intersection line, no residual dislocation is left on the GB; (2) direct slip transmission, a partial residual dislocation is left on the GB; (3) indirect transmission, , $\overrightarrow{b_1}$ and $\overrightarrow{b_2}$ are not parallel, a partial residual dislocation is left on the GB; (4) No transmission, the dislocations remain in the GB. For these scenarios, the residual Burgers vector magnitude $|\overrightarrow{b_r}|$ varies from zero for case (1) to higher values in cases (2) and 3 to a maximum for case (4). The magnitude of the residual Burgers vector is evaluated as follows:

$$|\overrightarrow{b_r}| = |\overrightarrow{b_1} - \overrightarrow{b_2}| \tag{3}$$

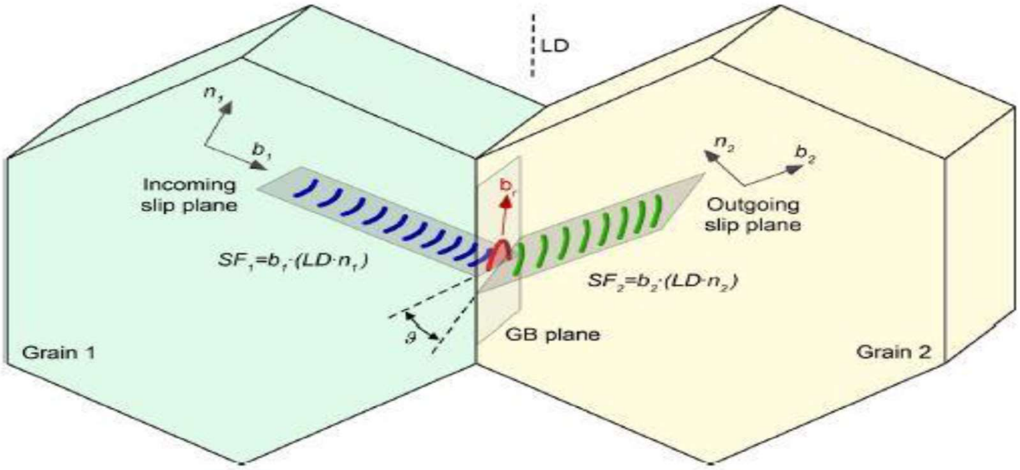

Figure 6. Schematic detailing the geometry of the dislocation – GB interaction (Patriarca et al., 2013).

The above criteria were applied to study the slip transmission in BCC FeCr polycrystal and high resolution strain measurements were taken and served to gauge the degree of GB strengthening and the $|\overrightarrow{b_r}|$ is used as a measure of the dislocation – GB interaction that takes place at the GB (Patriarca et al., 2013). It was observed that for $|\overrightarrow{b_r}| \rightarrow 0$, slip transmission is unaltered across the GB, the strain field is continuous and the contribution of the GB to material strengthening is minimal. For intermediate $|\overrightarrow{b_r}| <$ 1a where a is the lattice parameter, a step on the strain field is seen on the interface.

This step represents the slip accumulation on the incoming side of the GB. For high $|\overrightarrow{b_r}| > 1a$, slip accumulates at the GB and high strains are measured on the outgoing side of the GB.

The observation of dislocation interaction with LAGBs and HAGBs through in situ nanoindentation was performed by Ohmura(Ohmura et al., 2004). It was concluded that in the case of LAGB, the dislocations induced by the nanoindenter piled up against the boundary. A critical stress was reached as the indenter penetrated further into the grain. Which led to a high density of dislocations being emitted on the far side of the GB into the adjacent grain. As for HAGBs, no pileup was observed on the boundary, instead the dislocations produced by the indentation were absorbed into the boundary. Several models have been developed in order to investigate dislocation – GB interactions. 3D discrete dislocation dynamics (DDD) show that various mechanisms play a role in the transmission of dislocations through GBs. The ability for dislocations to penetrate GBs is quantified by calculating the penetration resistance stress for several types of lattice dislocations and by examining the type of interactions between incident dislocations and GB dislocations and how this interactions affects dislocation transmission through the boundary. In(Liu et al., 2011), five dislocation – GB interactions were examined: (1) Collinear annihilation: where two dislocations having collinear Burgers vectors on intersecting slip planes where the screw components annihilate (2) Mixed symmetrical junctions: two dislocations with Burgers vectors that are symmetrical with respect to the intersecting line of their respective slip planes (3) Mixed asymmetrical junctions: two dislocations with Burgers vectors that are asymmetrical with respect to the intersecting line of their respective slip planes (4) Edge junctions: two dislocations with Burgers vectors that are symmetrical with respect to the intersecting line of their respective slip planes, and (5) Coplanar: two dislocations on the same slip plane with different Burgers vectors. It was found that the main interaction happens when the incident dislocation and the GB dislocations interaction results in mixed symmetrical junction. This type of interaction results in the formation of a hexagonal network. A general LAGB, composed of two or more sets of mixed dislocations which is idealized as a perfect mesh constructed from two sets of dislocations that relax into a hexagonal network by forming binary junctions, is constructed using DDD and its interaction with an infinite dislocation is scrutinized(Liu et al., 2012). It was established that the LAGB poses a major obstacle to dislocation penetration with a wide span of resistances dependent on the slip system and line sense of the incoming dislocation as well as the mobility of GB binary junctions. These resistances, namely the stress required for a dislocation to transmit through the interface, the transmission stress, are directly related to the strength of the junctions formed between incident dislocations and the ones present in the GB. The dislocation – GB interactions were ranked from weakest to strongest, with the weakest being binary junctions formed by the interaction followed by ternary junctions, to collinear as the strongest interactions. The latter two reactions may result in an impenetrable boundary.

Multiscale modelling has also been used in an effort to understand the processes behind the deformation of polycrystalline materials. It is well understood that the GBs are the main factor in the plasticity of polycrystalline materials. Atomistic simulations coupled with continuum mechanics have been used in order to investigate edge dislocation – symmetric tilt boundary interactions, screw dislocations impinging on symmetric tilt boundaries and 60° dislocation pile-ups interacting with symmetric tilt GBs in FCC Al For the case of edge dislocations interacting with the GB, the governing deformation process is the nucleation of grain boundary dislocations (GBDs) at the dislocation – GB intersection. The pile-up of dislocation results in a modification in both the stress state and the residual defects at the intersection, the latter on account of dislocation absorption into the boundary. The deformation is irreversible when unloading the material and damage in the form of microvoids and loss of crystalline structure gathers around the intersection (M. P. Dewald & Curtin, 2007a). As for screw dislocations, upon impinging on the GB, a pile-up is formed along the GB which provides a back stress that requires increasing the applied load in order to drive the dislocations into the GB. Increasing the applied stress results in the nucleation of new screw dislocations in the opposite grain. Dislocation transmission is never observed even with large GBD pile-ups near the dislocation – GB intersection. The exact behavior of dislocations depends on the location of incident lattice dislocations and the extent of the pile-up. Transmission can occur on both Schmid and non-Schmid planes depending on the shear stresses on the GB plane (M. P. Dewald & Curtin, 2007b). The interactions between 60° dislocation pile ups with GBs were also examined in order to form a clear picture when it comes to dislocation – GB interactions. A set of criteria was developed in order to explain experimental observations, explain new mechanisms such as deformation twinning and formation of extended stacking faults, show that the reaction between incident dislocations and GBDs can be controlled by the leading partial of the incident dislocation instead of the full Burgers vector; and lastly to demonstrate that shear stresses and compressive stresses along the GB, GB dislocation processes influence the nucleation stress (M. Dewald & Curtin, 2011).

Upon loading lath martensite steels, the role of grain boundaries is apparent at high angle packet and block boundaries. Strain localization appears in the bulk of martensite blocks and at these boundaries in the form of interface plasticity. Another key factor that plays a role in lath martensite plasticity is the orientation of the boundary plane with respect to the loading direction. The most noticeable interface plasticity is for 45° orientations (Morsdorf et al., 2016).

D. Material Behavior Modeling

Over the years, significant progress has been made in computational and experimental methods to characterize and understand the microstructural behavior of polycrystalline materials, often computational and experimental methods are combined to form a clearer picture of material behavior. One such attempt includes crystallographic and experimental analysis coupled with models (Na et al., 2014) where multilayered steels consisting of two hard martensitic layers (low C and ultra-low C) and a ductile layer of austenite were used to study the correlation between slip system activation and the change in the microstructure of lath martensitic steel during tensile deformation up to 20% strain. At this level of strain, a refined microstructure was obtained. Formation of new substructures within blocks were observed due to the formation of new boundaries. In situ crystallographic analysis established that this phenomenon is due to inhomogeneous crystal rotation within individual blocks during deformation. A simple plasticity model was used in order to predict crystal rotation behavior and to track an activated slip system within a block during deformation. The experimental crystal rotation behavior and the simulated behavior were compared, both methods showed that the preferred slip system for activation is the in-lath slip system. The formation of deformation substructures becomes increasingly insignificant with increasing initial microstructure size indicating that the interaction between adjacent sub-blocks impacts crystal rotation behavior. Nambu (Nambu et al., 2009) used a typical tensile test specimen of the same multilayered steel at an engineering strain rate of 10^{-3} s^{-1}. TEM observation was performed to shed light on dislocation structure evolution during the deformation. True stress-strain plots showed a transition of the work hardening behavior. This is further validated through the use of X-ray diffraction analysis that showed a change in dislocation density in martensite with strain. Work hardening is enhanced when the applied strain exceeds 15-20% levels. Nano-indentation and micro-pillar compression tests are often used to characterize the mechanical properties pf materials, to that end Ghassemi-Armaki (Ghassemi-Armaki et al., 2014) conducted experiments using these two tests to acquire the micromechanical response of the martensite phase in a low carbon dual phase sheet steel. The overall stress-strain response was obtained from uniaxial tensile tests performed on dog-bone specimens extracted from the sheet. Micropillars were excised from the sheet before and after deformation, that is in the unloaded state and at two different strain levels. They were then subjected to compression tests conducted at a constant strain rate of 10^{-3} s^{-1}. The microstructure of the micropillars were examined in a TEM before and after deformation. The experiments confirmed that the yield strength of martensite is around 1 GPa and hardening occurs rapidly until 1.5 GPa followed by gradual hardening until 2.3 to 2.5 GPa. TEM observation showed that the onset of plastic flow and hardening will commence before the ultimate tensile strength is achieved in the dual-phase steel. Shin again used multilayered steels along with transformation induced plasticity steel with a large deformation above 20% strain (Shin et al., 2020) to predict the deformation of martensite. The martensitic deformation was investigated according to three key factors: 1) the size of prior austenite grains, 2)the alignment of blocks with a tensile axis and 3)the position of a block. The correlation between these three factors and activated slip systems was scrutinized using DAMASK (Roters et al., 2019), a crystal plasticity simulation kit in conjunction with EBSD scans that served as the microstructural input to the crystal plasticity model. The study found that block and sub-block boundaries increased in length smoothly during the deformation up to 20%. This significant increase in sub-block boundaries misorientation allows the drastic rotation of sub-blocks thus facilitating the large deformation of martensite. In an effort to understand the relationship between crystallographic features and the activity of local slip systems of as-quenched lath martensite multilayered steel during uniform elongation, Michiuichi (Michiuchi et al., 2009) found that during uniaxial tensile deformation of as – quenched lath martensite, the lath structure is maintained, and the lath-constrained slip systems are activated at less than 8% strain and subsequent hardening of primary slip systems becomes pronounced at 15% strain, confirming the results of the previous studies mentioned above. Shamsujjoha (Shamsujjoha, 2020) examined the role of solute carbon on the strengthening and work hardening behavior of lath martensite was analyzed by studying the microstructures of three low carbon martensite steels with different C contents. Uniaxial tensile tests were performed on samples taken from the three different steels. EBSD was used to study the microstructure in a Scanning Electron Microscope (SEM), X-ray diffraction was utilized to characterize the dislocation density of the samples before and after deformation. This study found that solute C atoms have little or no effect on the strain hardening of low C martensite. However, the block and lath width decreases with increasing carbon content. This decrease in lath width correlates with an increase in dislocation density. Block size is recognized as the effective grain size of lath martensite. Strengthening of lath martensite via dislocation rearrangement towards a stronger dipole character was perceived as the most dominant strengthening mechanism contributing up to 65% of the yield strength which in turn increases with increasing carbon content. The plasticity mechanisms of a fully lath martensite steel were investigated experimentally by Jo (Jo et al., 2017). The deformed steel showed a higher dislocation density than the as-received condition indicating dislocation multiplication during deformation. Lath martensitic steel are typically used in a power plant setting and are thus subjected to cyclic loading and fatigue, which leads to gradual cyclic softening.

In order to correctly simulate material stress – strain behavior, an appropriate material model must be selected. The use of these models allows the prediction of the mechanical response of a material to a given load. Modeling the behavior of polycrystalline materials is an arduous task that has been successfully attempted in the past, however, few attempts have been made to depict the hierarchical microstructure of martensitic steels in computational models. Due to the many length scales involved in martensitic steels, multiscale modeling, which involves bridging different scales together, is used to accurately represent the hierarchical microstructure. Li (D. F. Li et al., 2014a) used a finite element method (FEM) to explicitly simulate the microstructure and sub-micron precipitates of a P91 tempered martensitic steel. A dislocation mechanics and length scale dependent crystal plasticity model was used in (D. F. Li et al., 2014a) to account for slip based plastic deformation. The model also incorporates statistically stored dislocations (SSDs), that is dislocation multiplication based on random generation and recovery processes, and geometrically necessary dislocations (GNDs), which are dislocations accumulated in strain gradient fields caused by geometric constraints of the crystal lattice. The FE simulations were validated by use of uniaxial tensile test data at room temperature. A homogenization analysis was conducted in order to connect the different length scales present. It was found that the dislocation mean free paths depend on precipitate size and lath thickness and that using the homogenized model, polycrystalline simulations are able to predict the macroscopic effects that arise from softening due to precipitate and lath coarsening. The same model used in (D. F. Li et al., 2014a) in conjunction with a representative volume element (RVE) based on electron back-scatter diffraction (EBSD) scans were utilized to model the polycrystalline microstructure of a tempered martensite ferritic steel. In order to validate the model, three point bending experiments were carried out on a notched specimen manufactured from P91 steel with 20,000 h service history and tested at room temperature (Brian J. Golden et al., 2016). In order to capture the specimen level behavior at room temperature, the experimental data was used to generate an isotropic elastic-plastic model. The polycrystal model together with the EBSD data were used to scrutinize the material behavior in the vicinity of the notch root of the three point bending test. Excellent agreement was achieved between the model and the experimental data. The microstructure of P91 is complex with several levels of subgrains. Golden (B. J. Golden et al., 2014) examined two approaches to accurately represent the microstructure of a P91 martensitic steel used in power plants. One approach consisted of a representative microstructure that was generated using the Voronoi tessellation technique, a method commonly used to simulate the microstructure of polycrystalline materials. A 2D RVE is used in the generated microstructure method. The second method included preparing a sample of aged P91 for an SEM scan. EBSD was then performed on the prepared steel in order to accurately measure the microstructure. GBs are not explicitly incorporated within this model as these arise from the distribution of orientations determined from the EBSD scan. In both cases, the microstructural model is integrated with an RVE in a non-linear, rate dependent, finite strain crystal plasticity model which describes the material response. The models were calibrated to have identical global response but forecast different local stress and strain distributions at the microscale. However, the predicted differences are small, thus component predicted using a generated microstructure should not notably differ from those obtained using a measured microstructure. Sun (Sun et al., 2018) investigated the microscale deformation of a P91 steel using the FE method, the hierarchical microstructure was obtained experimentally by EBSD. An RVE was generated using a modification of the centroidal Voronoi tessellation (VT). A non-linear, rate dependent, finite strain crystal plasticity model is used to represent the mechanical response of the material at both the macro and micro-levels. Results have shown that through the use of the VT approach, block and packet boundaries do not affect the global material response, but strongly affect the local response.

Martensitic steels are known to soften during high temperature cyclic tests. This softening is explained by lath and sub-grain boundary elimination and a decreases in back stress. A study performed by Sauzay (Sauzay et al., 2005) attempts to model these phenomena. Three steps are involved in the modelling attempt. First the microstructure evolution is simulated. Second, the sub-grain back stress dependence, which was found from mechanical tests, with respect to the microstructure is laid out. And finally, sub-grain and block back stresses are computed along with the macroscopic stress for comparison purposes. The model proposed by Sauzay however is not considering other mechanisms which might take place during cyclic loading. One of the key contributions to loss of strength in martensitic steels under fatigue loading is cyclic softening which usually takes place in materials with a high initial dislocation density. A macro-scale constitutive model (Barrett et al., 2014) incorporating back-stress dependent strengthening mechanisms coupled with a dislocation based model for cyclic softening based on micromechanical phenomena such as LAGB dislocation annihilation. The model predicted that at low temperatures, a lath size effect on the plastic strain range and cyclic strength is present. That is, a smaller lath width gave a lower plastic strain range. However at higher temperatures, the model predicts rapid saturation of lath width and cyclic softening. Dundulis (Dundulis et al., 2017) carried out experimental testing of martensitic P91 steel under controlled strain conditions and at elevated temperature. Results show that P91 steel is characterized by cyclic softening and increasing rate of softening with an increase in strain amplitude. The same fatigue tests were simulated using a finite element plastic Chaboche isotropic stress hardening model showed that this kind of modeling can be carried out in case experimental testing cannot be performed. Li (D. F. Li et al., 2017) made use of a multiscale strain gradient crystal plasticity modelling framework to study cyclic plasticity and fatigue in a P91 tempered martensitic steel at elevated temperature, with grain and sub-grain features explicitly considered. The calculated stress-strain hysteresis loops showed good agreement with experimental data. The modelling results indicate that cyclic micro-plasticity is strongly dependent on lath size.

Due to the hierarchical structure of lath martensitic steels, very small length scales are involved, thus, the size effect comes into play and the size of effect of packet, block and lath boundaries must be investigated and its impact on mechanical response quantified. The effect of block size in lath martensitic steel was examined by Morito(Morito et al., 2006). The microstructure was characterized using SEM/EBSD and TEM. TEM observations along with a Hall-Petch type analysis revealed that the block size is the effective grain size and an important structural parameter when analyzing the relationship between strength and structure in lath martensite steels. Sun (Sun et al., 2019) investigated a P91 martensitic steel using a strain gradient crystal plasticity model implemented using the Voronoi Tessellation method to model the hierarchical structure i.e. prior austenite grain PAG/packet/block and the effect of the PAG/packet/block size on the macro and micro-scale mechanical behavior. The role of lath interaction and the influence of dislocation type (statistically stored and GND) is also studied. Results showed that the effect of lath misorientation on the tensile response is negligible. The composition of the initial statistically stored dislocations and GNDs does not influence the yield strength and flow strength of the material. The block diameter was found to be the dominant microstructural length scale which affects the size dependent behavior of the yield strength, the flow stress and shear band width. This is further confirmed by Li (S. Li et al., 2016) who found that the yield strength decreased with increased packet size and block width according to a Hall – Petch relationship. Another study conducted by Luo (Luo et al., 2020) on the influence of refined hierarchical martensitic microstructures on the yield strength concluded that the effective grain size can be defined by the high angle grain boundaries, namely the prior austenite grain boundaries and the packet and block boundaries. The previously mentioned studies have focused solely on blocks and packets and have not made laths their main focus.

E. Summary

A review of dislocation – grain boundary interactions is presented. The many different experimental and computational techniques relevant to mechanical characterization of high temperature power plant materials is presented. The concepts covered can be summarized as follows:

- Characteristics of martensitic steels.
- Dislocation – grain boundary interactions from a computational perspective and an experimental point of view.
- A review of relevant material models and experimental techniques to characterize plasticity of martensitic steels.

However, clear gaps in the literature relate to dislocation interaction with lath boundaries in martensitic steels and how this interaction contributes to the overall material behavior. Previous work relating to characterizing the response of lath martensitic steels has been carried out mainly using crystal plasticity models. This study aims to address these gaps using a multi-scale dislocation dynamics approach.

CHAPTER III

METHODOLOGY

This chapter outlines the methodology and the underlying physical processes and equations used in this work. The first section deals with the dislocation dynamics framework, the second section details the construction of the low angle lath boundaries and finally, the third section describes the Kurdjumov – Sachs crystallographic orientation relationship present in martensitic steel and its implementation in the dislocation dynamics framework.

A. MDDP

MDDP is a hybrid elasto-viscoplastic simulation model coupling DDD with finite element (FE) analysis. DDD is used to determine plastic deformation in single crystals by the evaluation of the dislocation evolution history. Dislocation lines and curves are represented by discrete straight segments. At each time step, the Peach-Koehler (PK) force is computed by accounting for all force components arising from: Peierls barrier ($F_{Peierls}$), dislocation-dislocation interaction (F_D), self-force (F_{self}), interaction with obstacles ($F_{obstacle}$), image forces (F_{image}), and externally applied loads ($F_{External}$). Thus the total glide force on each dislocation segment *i* can be expressed as:

$$F_i = F_{Peierls} + F_D + F_{self} + F_{External} + F_{obstacle} + F_{image} \tag{5}$$

The dynamics of dislocations is governed by a “Newtonian” equation of motion, consisting of an inertia term, viscous damping term, and driving force term such that,

$$m_i \dot{v}_{gi} + \frac{1}{M_i} v_{gi} = F_i \tag{6}$$

In the above equations, m_i is the effective dislocation segment mass, M_i is the dislocation mobility which depends on the dislocation segment orientation, v_{gi} is the segment glide velocity. The equation of motion is then solved to find the velocities and thus the plastic strain rate $\dot{\varepsilon_p}$ and the plastic spin W_p are evaluated respectively:

$$\dot{\varepsilon}^p = \sum_{i=1}^{N} \frac{l_i v_{gi}}{2V} \left(n_i \otimes b_i + b_i \otimes n_i \right) \tag{7}$$

$$W^p = \sum_{i=1}^{N} \frac{l_i v_{gi}}{2V} \left(n_i \otimes b_i - b_i \otimes n_i \right) \tag{8}$$

Where l_i is the dislocation segment length, n_i is a unit normal to the slip plane, and V is the volume of the representative element. The above relations provide the most rigorous connection between the dislocation motion (the fundamental mechanism of plastic deformation in crystalline materials) and the macroscopic plastic strain, with its dependence on strength and applied stress being explicitly embedded in the calculation of the velocity of each dislocation.

In the macro level, it is assumed that the material obeys the basic laws of continuum mechanics, *i.e.* linear momentum balance and energy balance:

$$div\,\mathrm{S} = \rho\, \dot{\mathrm{v}} \tag{9}$$

$$\rho\, \mathrm{C_v} \dot{\mathrm{T}} = \eta\ \mathrm{S}.\dot{\varepsilon}^{\mathrm{p}} \tag{10}$$

In the above equations, S is the Cauchy stress tensor, T is the temperature, v_p is the particle velocity, ρ, C_v and K are mass density, specific heat, and thermal conductivity, respectively. For elasto-viscoplastic behavior, the strain rate tensor $\dot{\varepsilon}$ is decomposed into an elastic part $\dot{\varepsilon_e}$ and plastic part $\dot{\varepsilon_p}$ such that:

$$\dot{\varepsilon} = \dot{\varepsilon}^{e} + \dot{\varepsilon}^{p} \tag{11}$$

The elastic response is expressed using the incremental form of Hooke's law such that:

$$\overset{\circ}{\mathrm{S}} = \left[\mathrm{C}^{e}\right]\left[\dot{\varepsilon}^{e}\right] \tag{12}$$

Where C^e is the anisotropic elastic stiffness tensor. Combining (10) and (11) leads to:

$$\overset{\circ}{S} = \left[C^{e}\right]\left[\dot{\varepsilon} \text{-} \dot{\varepsilon}^{p}\right] \tag{13}$$

To correct for the actual boundary conditions when coupling DD with FE, the principle of superposition is applied. The dislocations contained within the RVE produce an internal stress and the effective total stress within the RVE is the sum of all internal stresses and any externally applied stress. Thus, the long-range stresses are treated as internal variables which leads to an efficient numerical scheme. With this approach, complex dislocation structures with mixed boundary conditions are easily dealt with. Details of the MDDP framework can be found in (Zbib & Diaz de la Rubia, 2002).

B. Geometry & Material Parameters

To model the behavior of martensitic steels, a Burgers vector of $b = 2.48$ Å corresponding to iron is used (the carbon solute atoms are ignored in MDDP). A shear modulus of $G = 78$ GPa is adopted with a Poisson's ratio of 0.34. A discretization length of $50b$ is used. Edge dislocation mobility is set as $M_{edge} = 10^3$ Pa^{-1}s^{-1} whereas the screw dislocation mobility is amplified by a factor of 100 so as to mimic the behavior of a real BCC crystal, that is, $M_{screw} = 10^5$ Pa^{-1}s^{-1}. A mass density of 7800 kg/m^3 is used. Periodic boundary conditions are adopted to model dislocation motion and interaction in bulk crystals. That is, when a dislocation segment leaves a surface, it emerges from the opposite side of the RVE. These parameters will be used throughout this study.

C. Lath Boundaries

Two low angle tilt boundaries are constructed for the MDDP simulations in order to simulate a lath substructure. The boundary width is equal to the RVE width in both the x and y directions. The dislocation lines are parallel to the $x-$axis and the Burgers vector is oriented so as to obtain pure edge dislocations. The GB configuration and the boundary conditions are shown in **Fig. 7** where L_x and L_y are fixed to 2μm and L_z is twice the lath width D in order to maintain periodicity. $\frac{1}{2}\,[\bar{1}\;1\;\bar{1}]$ dislocations on a $(1\;1\;0)$ slip plane are piled up to form the GB. Each GB dislocation is separated by a distance $d = 250b$ which corresponds to 71.5 nm. The misorientation angle θ is calculated by the use of (1) and was found to be 0.23°. A single Frank – Read prismatic source placed on the (011)[$\bar{1}\;\bar{1}$ 1] slip system which has the highest Schmid factor of 0.4, acts as a dislocation generation mechanism that can move via glide only. **Table 2** shows the slip system for the GB dislocations and the Frank – Read source along with the corresponding indices used to represent them in MDDP. The reference frame has been rotated as shown below in order to properly construct the LAGBs as the MDDP requires that the z axis be normal to the plane where the GB dislocations are located, and that the x axis is in the direction of the line sense of the GB dislocations. The discretization length for the dislocation segments is 50b, that is 0.0124μm and periodic boundary conditions are used since a very small fraction of the material is being considered.

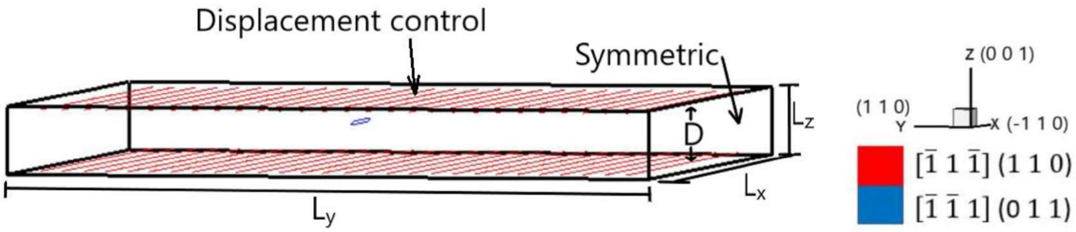

Figure 7. RVE schematic showing the simulation setup along with the boundary conditions. Shown here are two LAGBs separated by a distance $D = {}^{L_z}/_{2}$.

Table 2. LAGB dislocations' slip system with the matching MDDP indices.

Slip plane #	Burgers vector	Plane index	Vector index
(**1 1 0**)	$[\bar{1}\,1\,\bar{1}]$	5	2
(0 **1 1**)	$[\bar{1}\,\bar{1}\,1]$	2	3

D. Kurdjumow – Sachs orientation relationship implementation

The transformation mechanism from austenite to martensite in the K – S relationship is based on shear and rotation. The K – S orientation relationship describing the transformation from austenite (γ) to martensite (α') is expressed as follows: $\{111\}_{\gamma}$ // $\{110\}_{\alpha'}$, $< 110 >_{\gamma}$ // $< 111 >_{\alpha'}$.

The $\{111\}_{\gamma}$ and $\{110\}_{\alpha'}$ correspond to the close packed slip planes of the austenite and martensite phases, respectively. Due to symmetry, cubic systems have 24 equivalent crystallographic variants in martensite which evolve from a single grain of austenite if the K – S orientation relationship is maintained. That is, 24 combinations of planes/directions that satisfy the K – S relationship. The crystallographic variants V_1, V_2, …, V_{24} are listed in **Table 3.**

The change in crystallographic orientation from austenite to martensite is expressed by a matrix equation:

$$\boldsymbol{M} = \boldsymbol{T}\boldsymbol{A}, \tag{14}$$

where $\boldsymbol{T}$ is the orientation transformation matrix, $\boldsymbol{M}$ and $\boldsymbol{A}$ are the orientation matrices made up of three orthogonal unit vectors indicating the crystallographic directions for the martensite and austenite phases, respectively (Kitahara et al., 2006). The misorientation angle between two different variants are calculated using the orientations for the 24 martensite variants ($\boldsymbol{M}_i$ where $i = 1,2, \dots 24$). The rotation matrix $\boldsymbol{R}$ between the $\boldsymbol{M}_1$ and $\boldsymbol{M}_2$ variants for example is calculated from the below equation:

$$\boldsymbol{M}_2 = \boldsymbol{R}\boldsymbol{M}_1. \tag{15}$$

According to **Table 3**, a maximum of six possible variants or blocks can appear in a single packet. Therefore, for this study, the RVE that will be used in this work is going to be divided in two as shown in **Fig. 8** below in order to represent a packet containing two martensite variants, namely, the $\boldsymbol{M}_1$ and $\boldsymbol{M}_2$ variants. The RVE is divided by a block boundary. The rotation matrix $\boldsymbol{R}$ is chosen such that the misorientation angle between the $\boldsymbol{V}_1$ and $\boldsymbol{V}_2$ variants is 60° according to Kitahara et al., 2006 as summarized in **Table 4**. That is, the rotation has to be such that when it is applied, the slip plane normal remains the same in both blocks, namely the (011) plane, and the Burgers vector rotates from the $[\bar{1}\bar{1}1]$ slip direction to the $[\bar{1}1\bar{1}]$ direction. In the current methodology, the crystallographic orientation, $\boldsymbol{M}_1$, for the $\boldsymbol{V}_1$ variant is chosen as $\boldsymbol{M}_1 = \begin{pmatrix} 1 & 0 & 0 \\ 0 & 1 & 0 \\ 0 & 0 & 1 \end{pmatrix}$, therefore if one is to adopt the $\boldsymbol{M}_2$ crystallographic orientation presented in Kitahara et al., 2006, then the mismatch between $\boldsymbol{V}_1$ and $\boldsymbol{V}_2$ would not be equal to 60°, that is because the original frame of reference used in the aforementioned work belongs to the crystallographic orientation of austenite, that is the original frame of reference before the martensitic transformation is $\begin{pmatrix} -0.707 & 0.408 & 0.577 \\ 0 & -0.816 & 0.577 \\ 0.707 & 0.408 & 0.577 \end{pmatrix}_{\gamma}$ which is not the case for MDDP where the reference frame used is $\begin{pmatrix} 1 & 0 & 0 \\ 0 & 1 & 0 \\ 0 & 0 & 1 \end{pmatrix}$. Therefore, in order to calculate the correct $\boldsymbol{M_2}$ for MDDP to obtain the correct mismatch value of 60°, the authors had to make use of Kitahara et al., 2005, where the original reference frame used is the same as that of MDDP. By making use of the previously mentioned research, the authors were able to obtain $\boldsymbol{R} = \begin{pmatrix} -0.5 & 0.612 & -0.612 \\ -0.612 & 0.25 & 0.75 \\ 0.612 & 0.75 & 0.25 \end{pmatrix}$ and the crystallographic orientation $\boldsymbol{M_2}$ corresponding to the $\boldsymbol{V_2}$ variant was found to be $\boldsymbol{M_2} = \begin{pmatrix} -0.5 & 0.612 & -0.612 \\ -0.612 & 0.25 & 0.75 \\ 0.612 & 0.75 & 0.25 \end{pmatrix}$. The mismatch between $\boldsymbol{V_1}$ and $\boldsymbol{V_2}$ was calculated by using the dot product formula between the slip direction of $\boldsymbol{V_1}$, namely $\overrightarrow{b_1}$ = [-0.577 -0.577 0.577], and $\boldsymbol{V_2}$ which has now been rotated with respect to $\boldsymbol{V_1}$ to obtain a slip direction $\overrightarrow{b_2}$ = [-0.418 0.642 0.642]. The mismatch was found to be 60° as reported in Kitahara et al., 2006.

The packet and block boundaries are modeled as frictional stresses imposed in the RVE at the specified locations, the value of the frictional stresses are based on the findings of Shibata et al., 2010 on the yield strength of samples with blocks boundaries and packet boundaries. The reasoning is that high angle grain boundaries are impenetrable GBs and are therefore modeled as high friction barriers. **Fig. 8** showcases the RVE used, and the periodic boundary conditions adopted. Note that, as many blocks can be added to the RVE by modifying the MDDP code and using the correct $\boldsymbol{R}$ matrices for the corresponding variants that will be added.

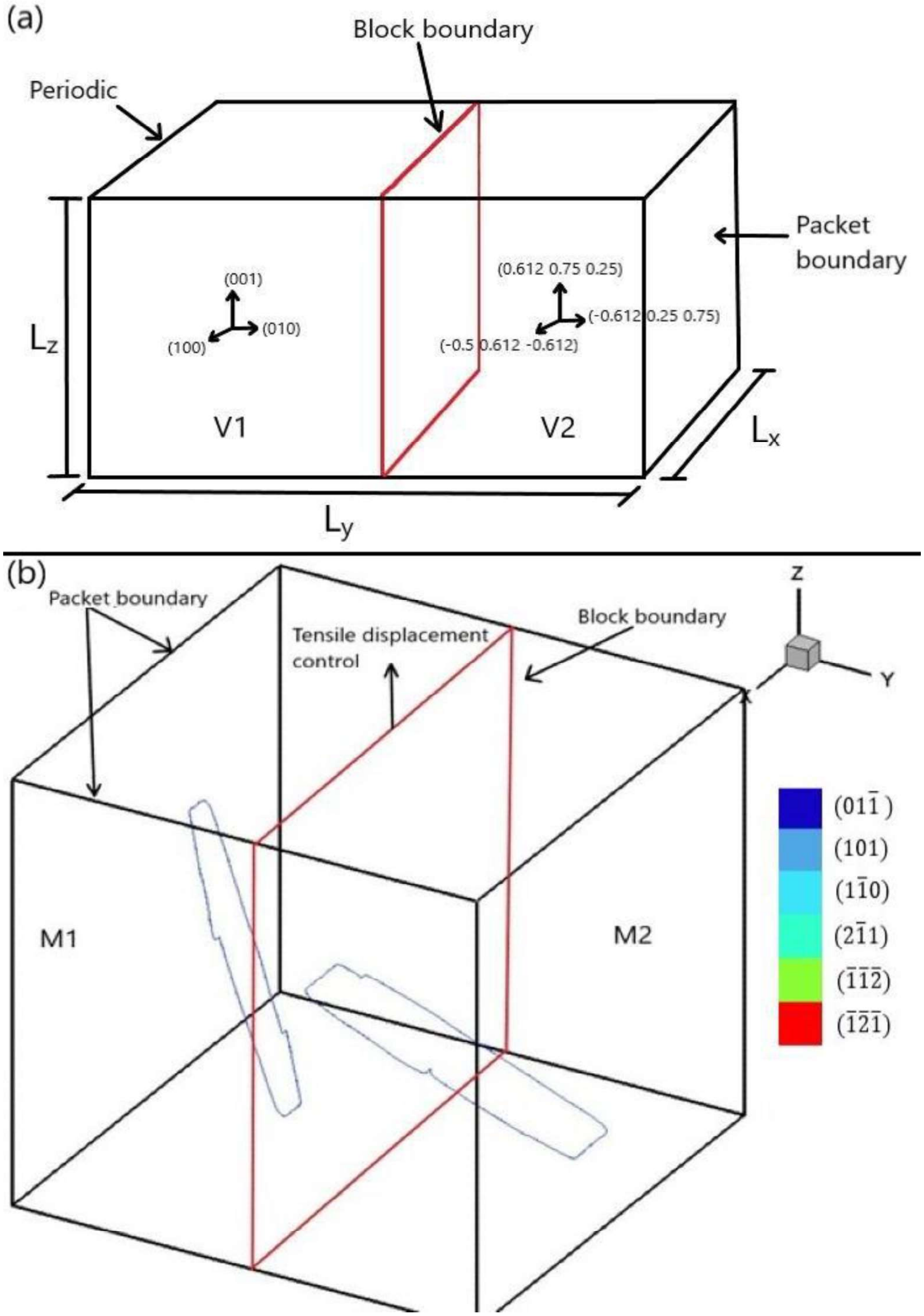

Figure 8. (a) Schematic showing the simulation setup with the crystallographic orientation. (b) Detailed simulation setup depicting the packet containing two FR sources (blue) enclosed by packet boundaries (black lines) and divided into two blocks by a block boundary (red lines). Packet and block boundaries are modelled as high frictional barriers. The samples are subjected to uniaxial tension with periodic boundary conditions.

Table 3. The 24 crystallographic variants for the K - S orientation relationship (Kitahara et al., 2006).

Variant	Plane parallel	Direction parallel
V1	$(111)_{\gamma}//(011)_{\alpha'}$	$[\bar{1}01]_{\gamma}//[\bar{1}\bar{1}1]_{\alpha'}$
V2		$[\bar{1}01]_{\gamma}//[\bar{1}1\bar{1}]_{\alpha'}$
V3		$[01\bar{1}]_{\gamma}//[\bar{1}\bar{1}1]_{\alpha'}$
V4		$[01\bar{1}]_{\gamma}//[\bar{1}1\bar{1}]_{\alpha'}$
V5		$[1\bar{1}0]_{\gamma}//[\bar{1}\bar{1}1]_{\alpha'}$
V6		$[1\bar{1}0]_{\gamma}//[\bar{1}1\bar{1}]_{\alpha'}$
V7	$(1\bar{1}1)_{\gamma}//(011)_{\alpha'}$	$[10\bar{1}]_{\gamma}//[\bar{1}\bar{1}1]_{\alpha'}$
V8		$[10\bar{1}]_{\gamma}//[\bar{1}1\bar{1}]_{\alpha'}$
V9		$[\bar{1}\bar{1}0]_{\gamma}//[\bar{1}\bar{1}1]_{\alpha'}$
V10		$[\bar{1}\bar{1}0]_{\gamma}//[\bar{1}1\bar{1}]_{\alpha'}$
V11		$[011]_{\gamma}//[\bar{1}\bar{1}1]_{\alpha'}$
V12		$[011]_{\gamma}//[\bar{1}1\bar{1}]_{\alpha'}$
V13	$(\bar{1}11)_{\gamma}//(011)_{\alpha'}$	$[0\bar{1}1]_{\gamma}//[\bar{1}\bar{1}1]_{\alpha'}$
V14		$[0\bar{1}1]_{\gamma}//[\bar{1}1\bar{1}]_{\alpha'}$
V15		$[\bar{1}0\bar{1}]_{\gamma}//[\bar{1}\bar{1}1]_{\alpha'}$
V16		$[\bar{1}0\bar{1}]_{\gamma}//[\bar{1}1\bar{1}]_{\alpha'}$
V17		$[110]_{\gamma}//[\bar{1}\bar{1}1]_{\alpha'}$
V18		$[110]_{\gamma}//[\bar{1}1\bar{1}]_{\alpha'}$
V19	$(11\bar{1})_{\gamma}//(011)_{\alpha'}$	$[\bar{1}10]_{\gamma}//[\bar{1}\bar{1}1]_{\alpha'}$
V20		$[\bar{1}10]_{\gamma}//[\bar{1}1\bar{1}]_{\alpha'}$
V21		$[0\bar{1}\bar{1}]_{\gamma}//[\bar{1}\bar{1}1]_{\alpha'}$
V22		$[0\bar{1}\bar{1}]_{\gamma}//[\bar{1}1\bar{1}]_{\alpha'}$
V23		$[101]_{\gamma}//[\bar{1}\bar{1}1]_{\alpha'}$
V24		$[101]_{\gamma}//[\bar{1}1\bar{1}]_{\alpha'}$

Table 4. Misorientation angles between V1 and the other martensitic variants (Kitahara et al., 2006)

Variant	**Misorientation angle from V1**
V1	-
V2	60
V3	60
V4	10.53
V5	60
V6	49.47
V7	49.47
V8	10.53
V9	50.51
V10	50.51
V11	14.88
V12	57.21
V13	14.88
V14	50.51
V15	57.21
V16	20.61
V17	51.73
V18	47.11
V19	50.51
V20	57.21
V21	20.61
V22	47.11
V23	57.21
V24	21.06

CHAPTER IV

LATH BOUNDARIES

This chapter outlines in detail the results of the lath simulations presented Chapter III. First, the findings of the loading process are presented in terms of stress strain diagram, and microstructure evolution. Then, these results are discussed, and main microstructural features are scrutinized. Size effect in lath martensitic steels is investigated when the effective grain size is taken as the lath width. Finally, the main findings are summarized at the end of this chapter.

A. Stress – Strain Behavior

Fig. 9 shows the stress and strain diagram for the simulated lath widths ranging between 0.2 μm and 0.5μm at a constant strain rate of 10^5 s^{-1} at 300 K. Inspecting the stress – strain behavior reveals the following:

1. Initially, the behavior is linear elastic up to the onset of yielding, which is between 1200 MPa and 1100 MPa, as seen in **Fig. 9a.** Yielding is followed by instantaneous stress relaxation. The stress exhibits an elastic overshoot followed by the detected drop in the yield stress implying that plastic relaxation took place.
2. Following yielding, plastic flow is initiated at ~ 700 MPa. Gradual strain hardening is observed up until ~ 2% strain. The plastic regime is characterized by a serrated curve as can be seen in **Fig. 9b.** These serrations are attributed to dislocation – GB interactions which will be examined in detail in section 4.2.
3. By plotting the plastic regime of the stress – strain diagram for each lath width starting at 1% strain, and by fitting the data according to the Hollomon law

(Atkinson, 1984) $\sigma = K\varepsilon^n$ where K is the strain hardening coefficient which serves as a proportionality constant and n is the strain hardening exponent, which is a measure of plastic deformation that lies between 0 (indicating a perfectly plastic material) and 1 (a perfectly elastic solid); most metals have a value n between 0.1 and 0.5. It can be seen that once plastic flow is initiated; hardening takes place as indicated by the strain hardening coefficient reaching 1 GPa and the hardening exponent shown in **Table 5**. The constants K and n for all cases can be found in the table below. It is worth noting that the difference between the strain hardening exponent n for the considered lath widths is not that large, i.e. the difference is smaller than 0.1, meaning that some hardening did indeed take place, prompting the authors to investigate any size effects using the lath width as effective grain size.

Table 5. Hollomon equation constants for considered lath widths.

Lath width (μm)	***K* (GPa)**	***n***
0.2	1	0.15
0.3	1	0.13
0.4	1	0.14
0.5	1	0.12

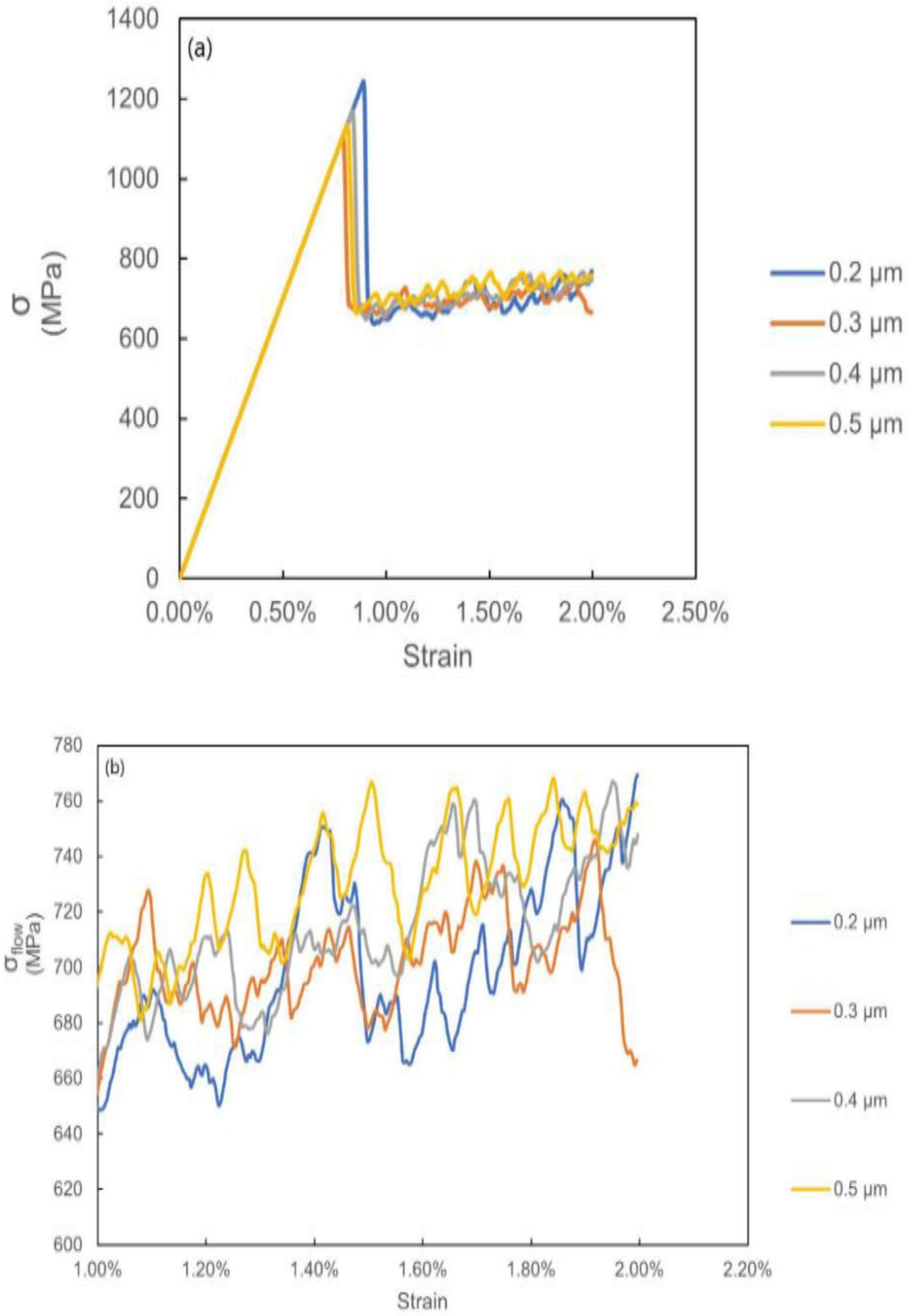

Figure 9. (a) Stress – strain diagram showing the material response to applied load. (b) Plastic regime of the material showing serrations in the stress – strain curve which are attributed to dislocation – GB interactions.

B. Microstructure and dislocation density evolution

Snapshots of the dislocation microstructure from a sample simulated at 10^5 s^{-1} strain rate at room temperature are shown in **Fig. 10**. Initially, two LAGBs are constructed by piling up pure edge dislocations on the (1 1 0) slip plane, and a single prismatic FR source is placed between the LAGBs and is situated on the (0 1 1) slip plane. Once the FR source activated, the generated dislocations will glide according to the $[\bar{1}\ 1\ \bar{1}]$ Burgers vector (see **Fig. 8**). Once the critical resolved shear stress is attained, the dislocations start to asymmetrically bow out as seen in **Fig. 10b** due to the difference in mobility and lattice friction between edge and screw components. As the loading proceeds, the first instance of a dislocation – GB interaction is observed, where upon first contact, the LAGBs prevent dislocation motion through them as can be seen in **Fig. 10c**. When the dislocation first touches the GB, it leaves a small step on the GB dislocation As the stress increases and reaches a critical level, the dislocation is released from its pinning point and penetrates the GB by increasing the size of the step on the GB as illustrated in **Fig. 10d** and causing local boundary plasticity. As the stress further increases in magnitude and reaches the yielding point, dislocations multiply, and the process mentioned above repeatedly takes place. The process of dislocation pinning – unpinning results in the serrations in the stress – strain diagrams of **Fig. 9**. In other words, after the first instance of dislocation – GB interaction and following dislocation multiplication, another dislocation will be pinned on the GB causing local plastic deformation in the form of a small step on the boundary where the dislocation – GB interaction took place. As the loading continues, the flow stress increases and once it reaches a critical value, the dislocation is unpinned and continues its motion through the sample as seen in **Fig. 11**. When the dislocation is unpinned, the stress magnitude dips slightly and then continues its increase until another dislocation is unpinned which results in another dip in stress. The process continues indefinitely until the loading is completed. Another interesting microstructural feature is the rearrangement of dislocations into dipole configurations, a configuration which leads to material hardening as shown in **Fig. 12**. However it is worth noting that some dipoles are not stable and disassociate as if they are unzipping as seen in **Fig. 13**. In the final microstructural configurations in **Fig. 14**, it can be seen that for smaller lath widths, the number of dipoles is significantly higher than the number of dipoles present in the 0.4 µm & 0.5 µm cases where in the larger lath widths, pile ups are present. The larger number of dipoles in the 0.2 µm & 0.3 µm cases is attributed to the GBs acting as walls that confine the dislocation motion in between those walls thus restricting the possible elastic interactions between dislocations and forcing them to adopt more energetically favorable configurations and interactions, namely dipole formation and dislocation annihilation. In contrast to this, the 0.4 µm & 0.5 µm cases, the GBs are further apart from each other therefore reducing the effect of their stress fields on the mobile dislocations making them free to interact in more ways than the smaller lath width cases. By examining the final microstructure of the 0.4 µm & 0.5 scenarios, it can be seen that in addition to dipole formation, pile ups can be seen in the upper left corner of the RVE. A snapshot of the pile up in the 0.5 µm case is shown in **Fig. 15**. The pile results in a compressive stress reaching up to 400 MPa.

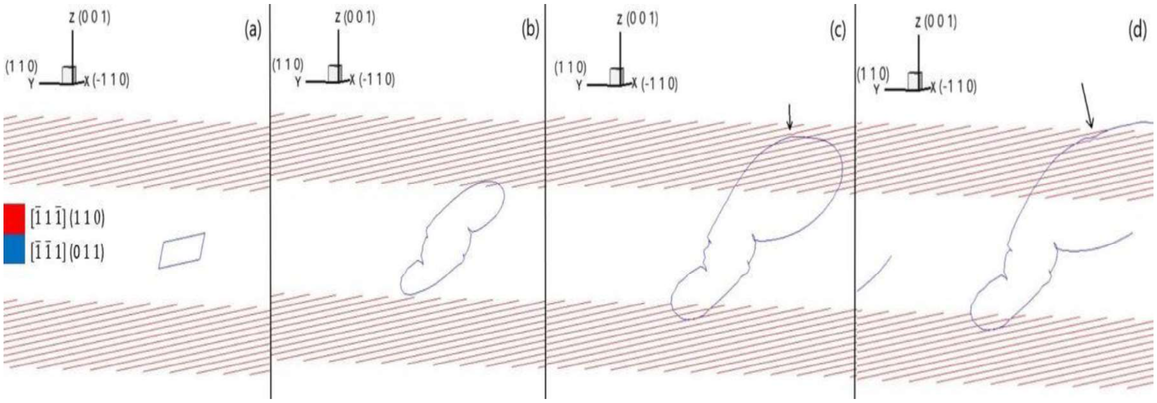

Figure 10. Snapshots of the GB-dislocation interaction. (a) Inactivated prismatic FR source, the color red corresponds to the GB while the blue corresponds to the FR source and the subsequent generated dislocations. (b) FR sources start to bow out asymmetrically due to the difference in the lattice friction and mobility between edge and screw components. (c) As the stress increases, the first instance of dislocation – GB interaction takes place where the dislocation gets pinned on the GB (shown with arrow). (d) Once the yield stress is reached, the dislocation is unpinned and penetrates the boundary causing local plastic deformation in the form of a small step on the GB.

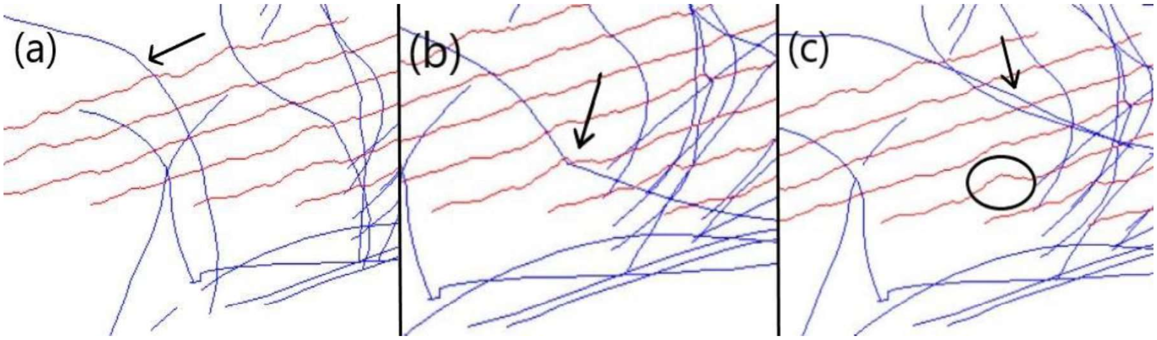

Figure 11. Snapshots of the dislocation pin/unpin process. (a) Incoming dislocation indicated by the arrow. (b) The dislocation is pinned on the GB causing a small step in the dislocation GB. (c) As the loading increases, the flow stress becomes high enough for the dislocation to penetrate the GB and continue moving through the crystal (indicated by the arrow) thus increasing the size of the step on the GB (indicated by the circle).

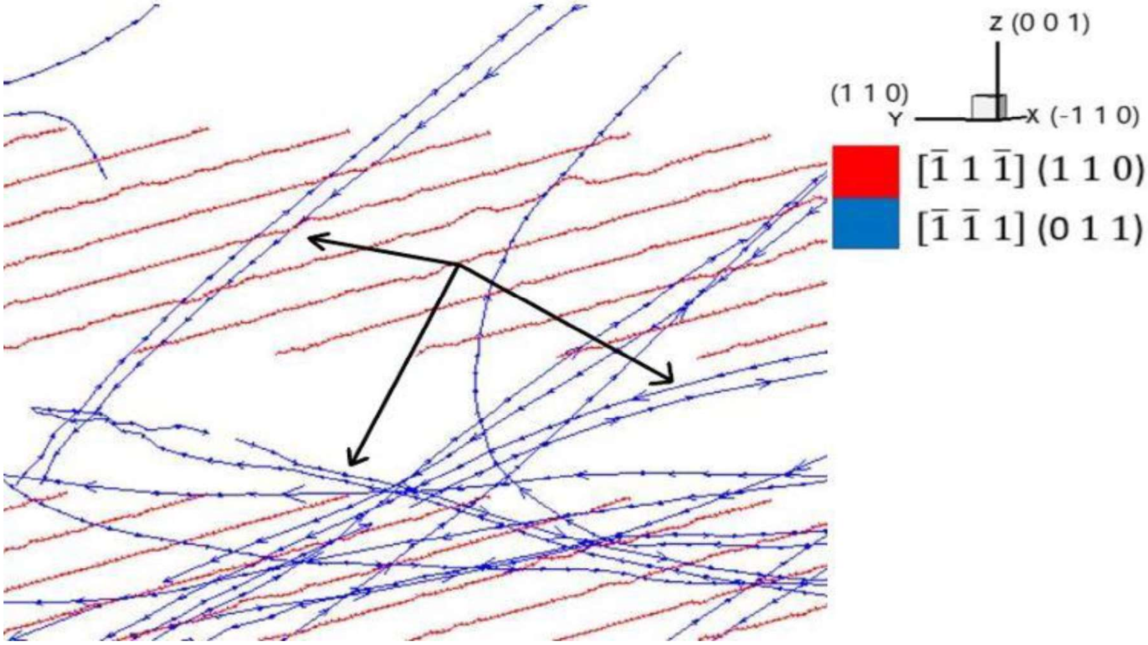

Figure 12. Dipole configuration which leads to hardening (shown with arrows.

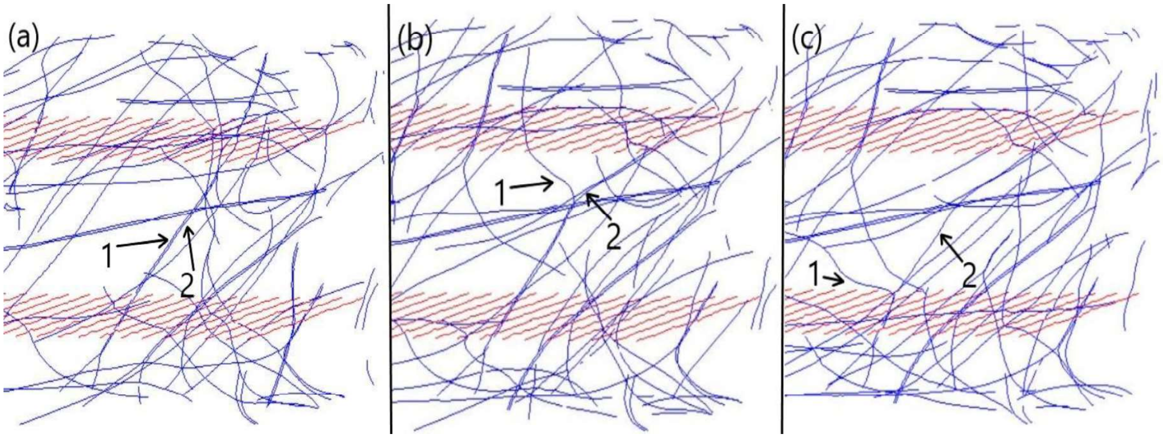

Figure 13. (a) Dislocations 1 and 2 in a dipole configuration. (b) Dislocation 1 starts to break away from dislocation 2 in an unzipping manner. (c) Dipole is disassociated.

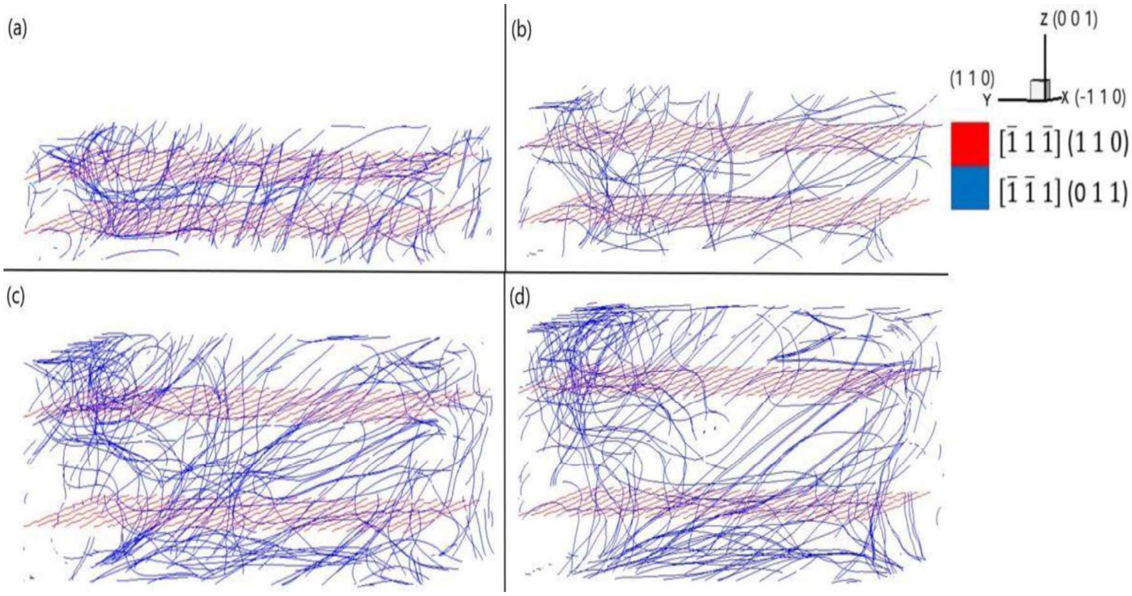

Figure 14. Final microstructural configurations for (a) 0.2 μm (b) 0.3 μm (c) 0.4 μm (d) 0.5 μm.

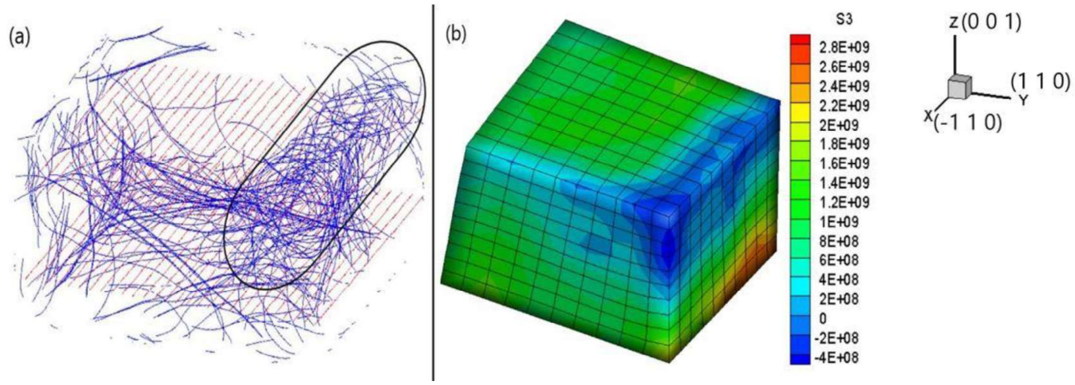

Figure 15. (a) Pile up (shown inside oval) snapshot taken from the 0.5 μm scenario (b) Stress contour showing the effect of the pile up (units in Pa).

The effect of the dislocation density over time is scrutinized by plotting the evolution of the dislocation density as a fucntion of time in **Fig. 15**. It can be observed that the dislocation densities follow a logarithmic trend in the form of $\rho = Alog(t) + B$, where ρ is the dislocation density, t is the time, A and B are fitting constants. By comparing the dislocation densities of the 0.3 μm, 0.4 μm and 0.5 μm lath width cases to the dislocation density of the smallest lath width scenario, namely the 0.2 μm case, it is seen that as the lath width increases, the dislocation density decreases. In other words, the smallest lath width, the 0.2 µm will have the largest dislocation desnity and as the lath width increases, the dislocation density will decrease until the 0.5 µm lath width scenario is reached where it will have the smallest dislocation desnity. This occurs because, as the lath width decreases, the volume of the sample will decrease and given the same number of dislocations at any given moment during the loading, there will be a higher dislocation density for the smaller volumes than the larger ones.

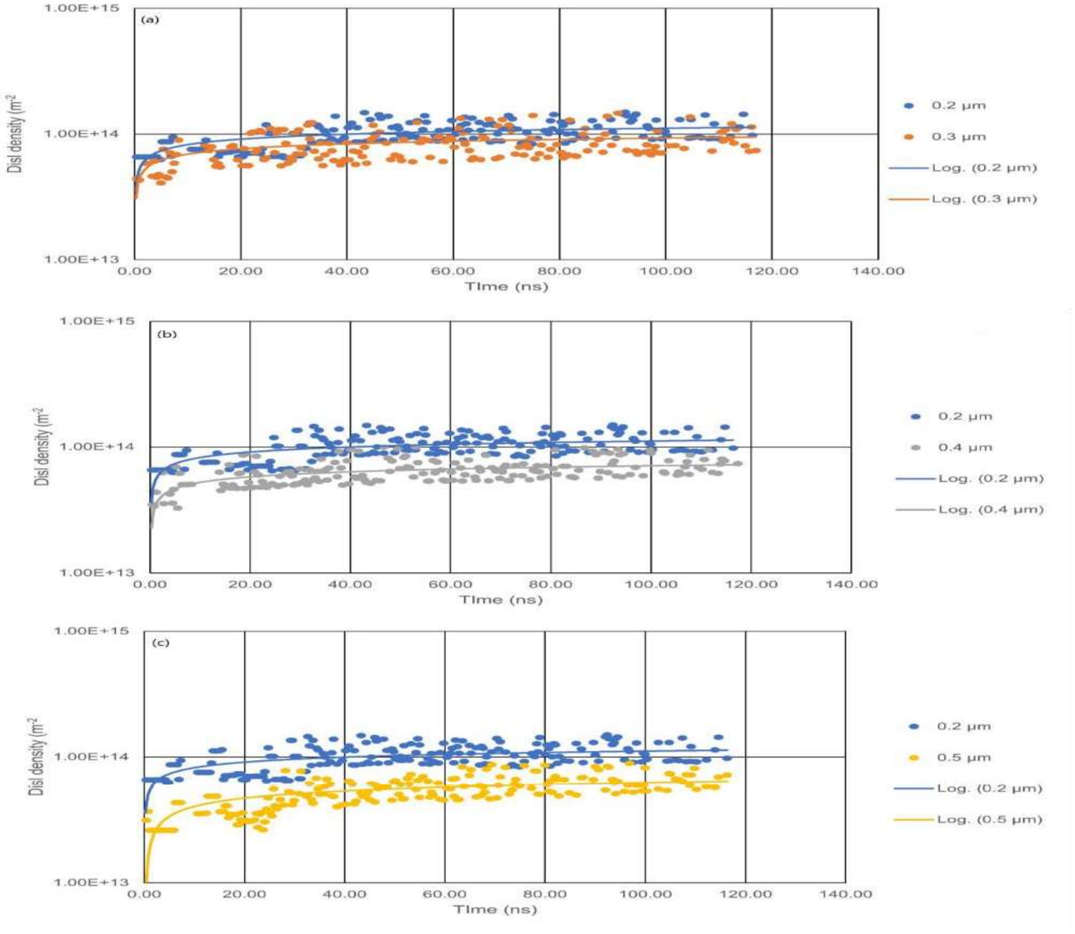

Figure 16. Dislocation density evolution over time comparison for (a) 0.2 µm & 0.3 µm (b) 0.2 µm & 0.4 µm (c) 0.2 µm & 0.5 µm

C. Size effect

By examining the flow stress at 1% strain, and by plotting it as a function of $1/\sqrt{D}$ as can be seen in **Fig. 17**, where D is the lath width, it can be seen that the flow stress does not follow a Hall – Petch dependency. Therefore, one can deduce that the lath width has no effect on the plasticity of lath martensitic steels. For that reason, the lath structure will be ignored in further simulations.

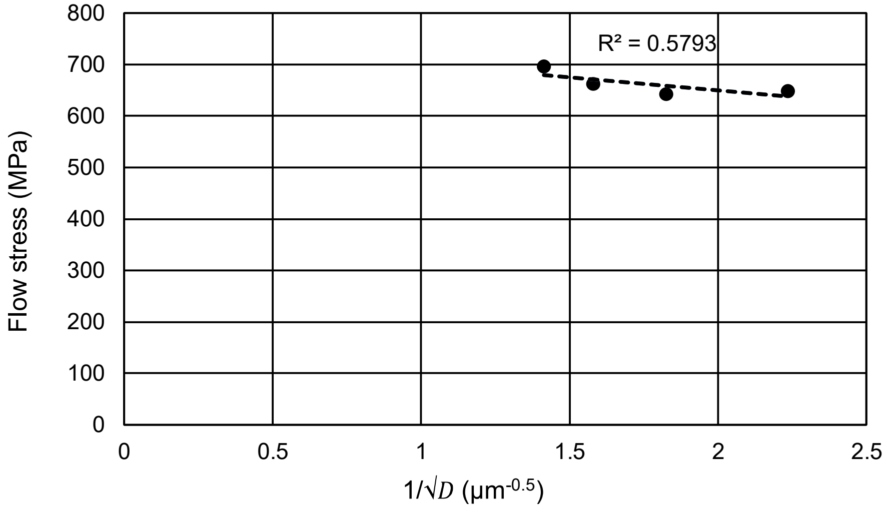

Figure 17. Flow stress vs $1/\sqrt{D}$.

D. Summary

The effect of lath width on the strength of martensite is examined by studying four lath widths and the interaction between dislocations and lath boundaries are scrutinized from a dislocation dynamics perspective. The results are summarized as follows:

1. The lath width is not a reliable effective grain size when considering size effect and Hall – Petch dependency.
2. Dislocations tend to rearrange themselves into a stronger dipole character. This mechanism is the most dominant in strengthening the material.

3. With increasing lath width, more dislocation interactions are possible since the GBs' stress fields does not act as restrictions to dislocation motion which makes pile – up possible.

CHAPTER V

K – S RELATIONSHIP IMPLEMENTATION

This chapter discusses the results of the implementation K – S orientation relationship, described in Chapter III, in MDDP. Different packet and block sizes are considered. Firstly, the mechanical behavior in response to uniaxial tension is investigated with regards to the stress strain diagram and the plastic strain evolution over time. Prominent microstructural features are extracted and related to the mechanical response.

A. Mechanical response

The K – S orientation relationship outlined in Chapter III was implemented as shown in **Fig. 8**. The RVE represents a packet which is divided into two blocks or variants, namely, the V1 and V2 variants. The considered block and packet sizes are shown in **Table 6** based on the findings of Sun et al., 2018.

Table 6. Size of the considered packets and blocks.

Packet size	Block size
2 µm	Two 1 µm blocks
3 µm	Two 1.5 µm blocks
4 µm	Two 2 µm blocks

Fig. 18a shows the stress strain diagram for the simulated packet – block combinations in **Table 5** at a constant strain rate of 10^5 s^{-1} at 300 K. By scrutinizing the mechanical behavior, the following features are revealed:

1. Initially, the behavior is linear elastic up to the onset of yielding.
2. Following yielding, plastic flow is initiated after a drop in stress via mass cross slip, i.e., a dislocation avalanche has taken place where secondary slip systems of the type <112> are activated, therefore indicating plastic relaxation.
3. Gradual strain hardening is observed afterwards due to the cross slipped dislocations piling up at both the packet and block boundaries. The effect of the hardening is balanced by relaxation processes, namely more cross slip, resulting in the stress magnitude being kept almost constant.
4. The samples undergo further relaxation. The process of relaxation is attributed to another cross slip event where dislocations cross slip on both the primary slip systems of the type <110> and secondary <112> slip systems of the type.

The dislocation avalanche and cross slip events are evidenced by observing how the dislocation density changes and evolves over time as is seen in **Fig. 18b**. Dislocation density starts to increase slightly once the critical resolved shear stress value is reached and the dislocations start to bow out and multiply through the FR mechanism. Yielding is marked by a sharp increase in dislocation density therefore evidencing the presence of a dislocation avalanche which can occur through cross slip. The dislocation density then reaches a plateau resulting in S – shaped dislocation density curves.

Upon initiation of plastic flow, it can be seen by examining the equivalent strain contour of the samples, that plasticity mainly occurs along bands. Sectioning the sample along the (100) plane as is seen in **Fig. 19a**, one can clearly observe that plasticity occurs along 45° bands in the [100] direction throughout the samples. The same can be said for plasticity in the [010] direction, by taking sections parallel to the (010) plane, plasticity occurs along bands that appear to be angled at around 30° throughout the samples also as shown in **Fig 19b**.

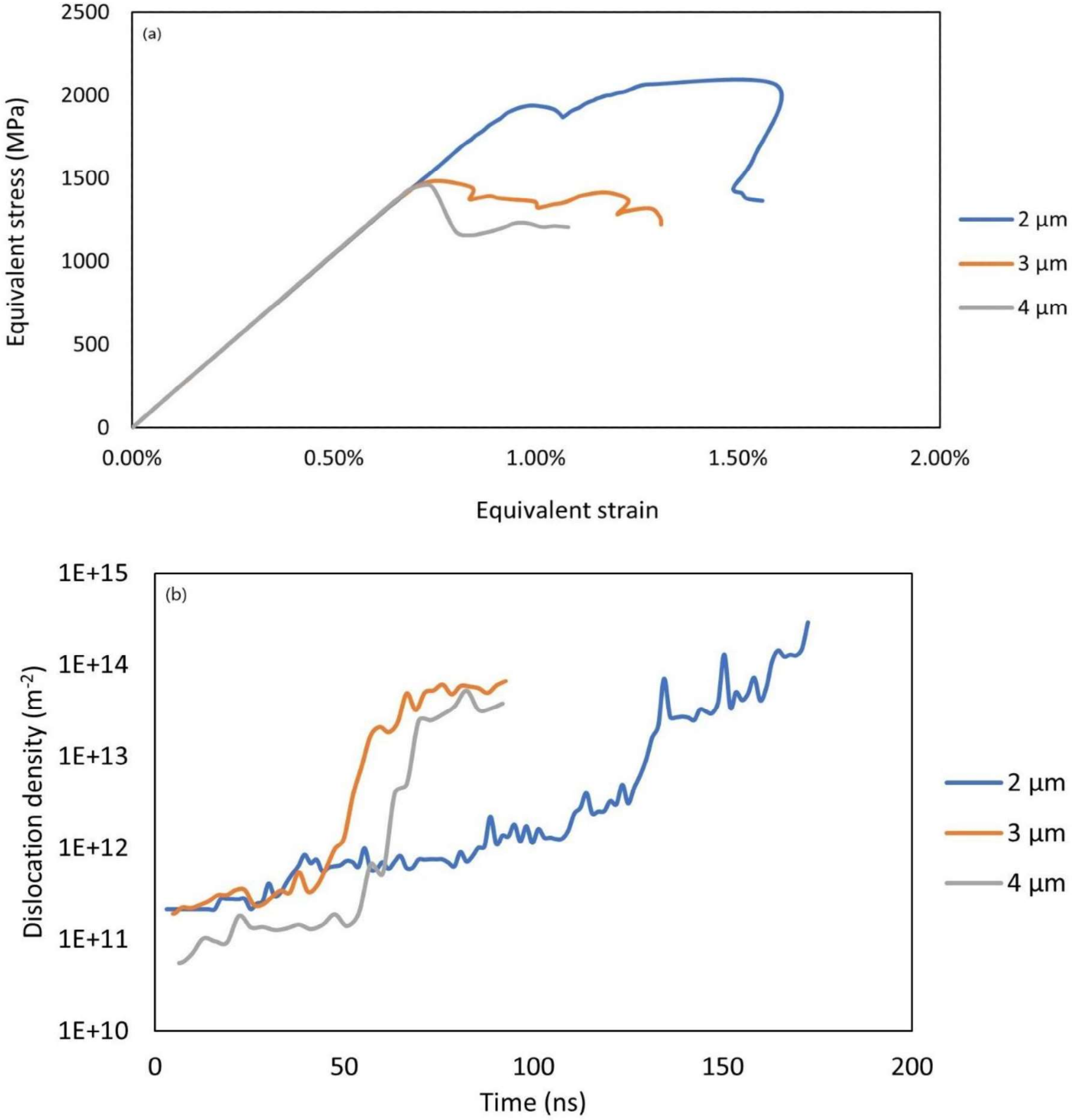

Figure 18. (a) Stress strain diagram depicting the mechanical response of the samples subject to uniaxial tension. The material is linear elastic up to yielding after which it undergoes plastic relaxation followed by a gradual hardening that is then followed by more relaxation. (b) Dislocation density evolution over time. Once dislocation multiplication takes place, the dislocation density slightly increases, which is followed by an abrupt surge in dislocation density which suggests that a dislocation avalanche has occurred. The dislocation density then plateaus until the next dislocation avalanche happens which results in another sharp increase.

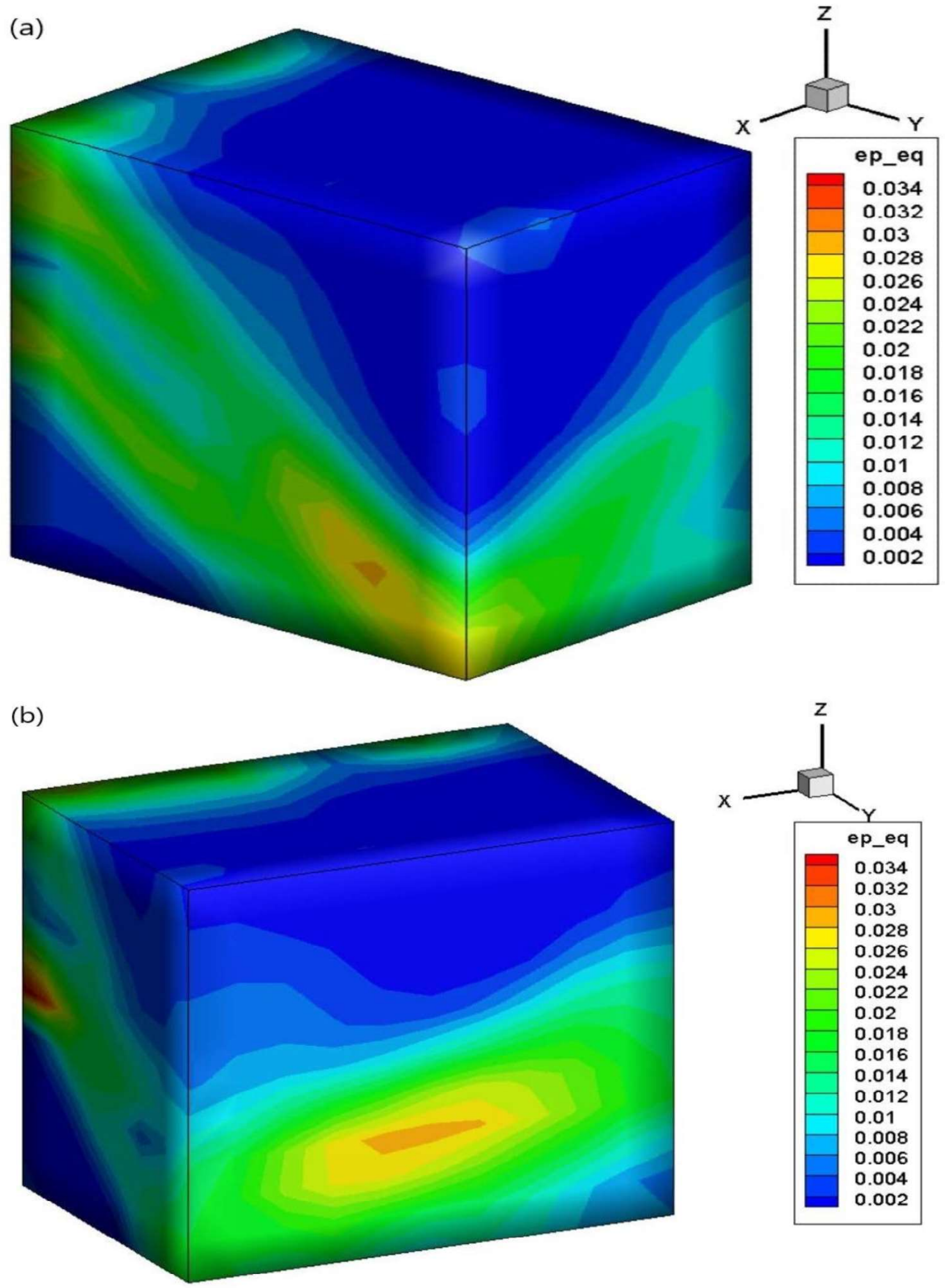

Figure 19. Equivalent plastic strain for 2 μm sample in (a) the [100] direction where plasticity manifests along 45° bands throughout the sample and in (b) the [010] direction where plastic bands form along 30° bands throughout the sample.

B. Microstructural features

The underlying microstructural processes govern and drive the mechanical response of the material at the macro scale. The features observed in the stress strain diagram and the evolution of the plastic strain can be traced back to the following main microstructural features:

1. Dislocation pile up at block and packet boundaries.
2. Cross slip resulting in dislocation avalanche.
3. Local deformation of grain boundaries due to dislocations penetrating the grain boundaries.

The first microstructural feature is first apparent before yielding takes place, namely the dislocation pile up shown in **Fig. 20**. Once the stress becomes high enough, the FR source bows out asymmetrically due to the BCC crystal structure. Once the critical resolved shear stress is reached, dislocation multiplication takes place, and the resulting dislocations start to pile up against the grain boundaries. Dislocations are piling up next to each other and as will be explained shortly, even on top of each other due to the hardening – relaxation process taking place in the samples.

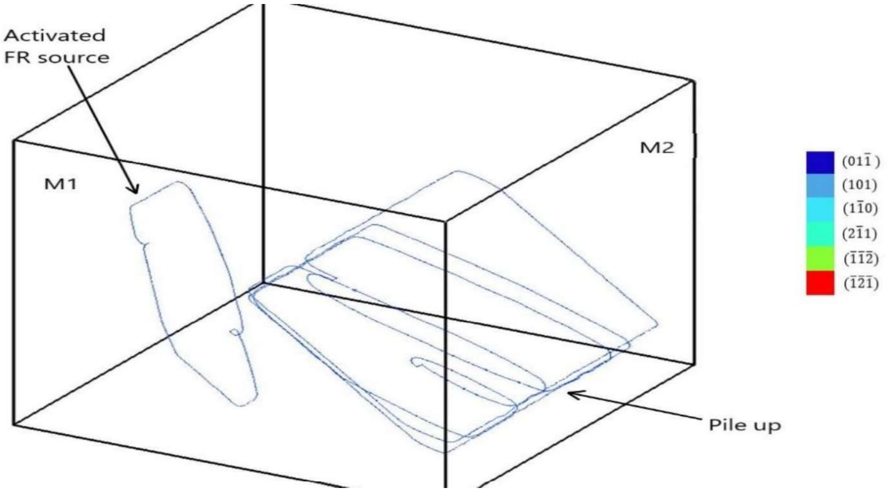

Figure 20. Frank – Read source activation and initial dislocation pile up.

As the stress increases, the second microstructural feature becomes apparent. Yielding occurs via dislocations undergoing mass cross slip where the $(\bar{1}\bar{1}\bar{2})$ and the $(\bar{1}\bar{2}\bar{1})$ secondary slip systems are activated resulting in a dislocation avalanche as seen in **Fig 21a**. These dislocations move through the crystal via glide motion and then pile up at the packet and block boundaries. As soon as plastic flow is initiated following yielding, dislocations glide freely through the crystal until they hit the grain boundaries and start piling up next to one another leading to some material hardening. The hardening is then balanced by a relaxation process in the form of cross slip where the dislocations emitted from the first dislocation avalanche effect themselves cross slip once again on the <110> and <112> slip planes only to once again pile up next to each other and on top of previously cross slipped dislocations as depicted in **Fig 21b** and **c** respectively.

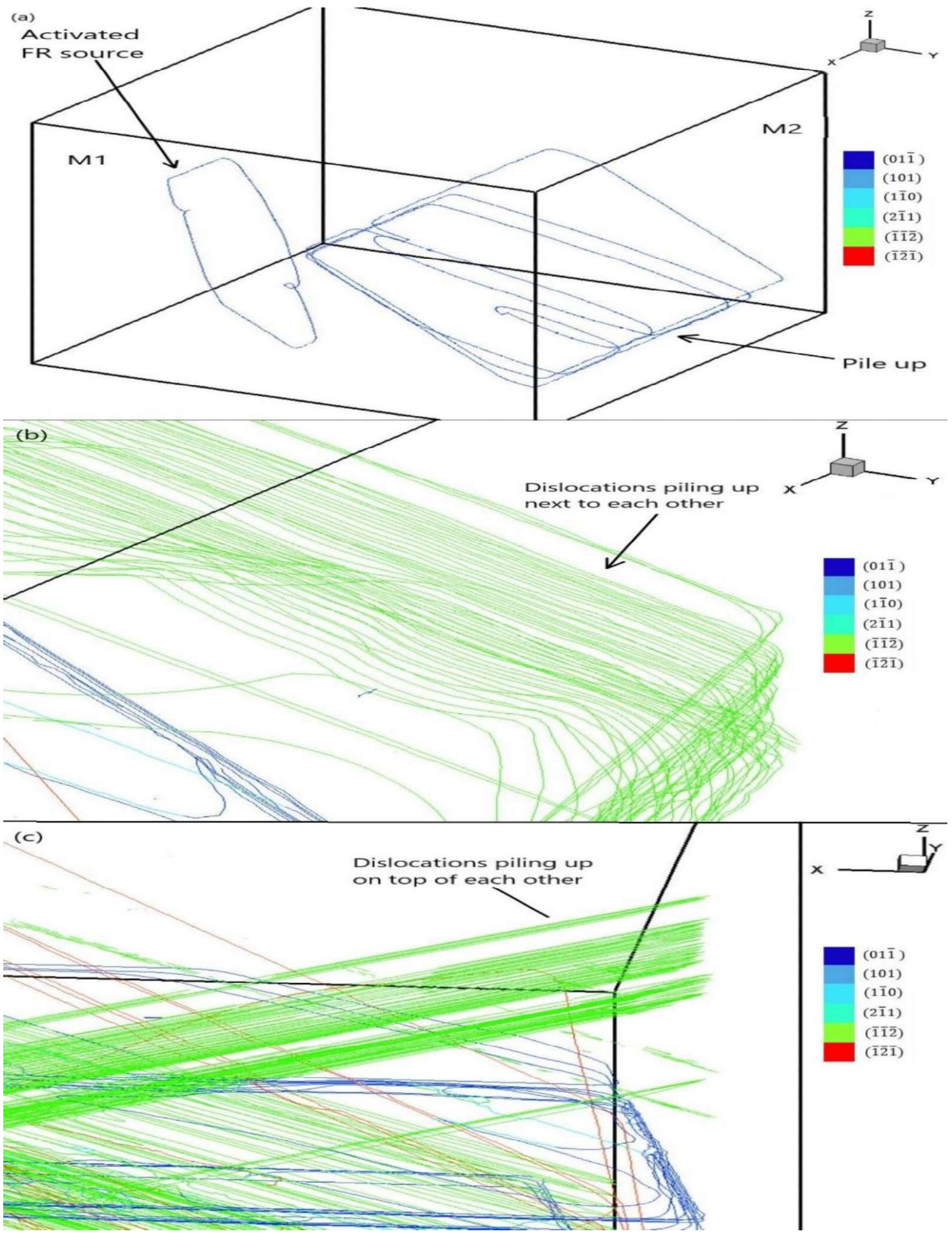

Figure 21. (a) Frank – Read source activation and initial dislocation pile up. (b) Cross slip which is responsible for dislocation avalanche leading to plastic relaxation in the samples. Cross slipped dislocations pile up next to each other against packet and block boundaries leading to material hardening. (c) Dislocations piling up on top of each other.

The continuous pile up of dislocations acts as a stress concentrator. The leading dislocation in the pile up containing n dislocations is subject to a forward force that propels it forward due to the resolved shear stress τ from the applied load and the other $(n-1)$ dislocations, and a backward force due to the internal stress τ_0 produced by the grain boundary. The leading dislocation along with the others move forward by a small distance δ. The applied stress does work per unit length of dislocation equal to $nb\tau\delta$. When the leading dislocation interacts with the grain boundary, the increase in the interaction energy between the leading dislocation and τ_0 is $b\tau_0\delta$. To maintain equilibrium, the stress experienced by the leading dislocation, τ_1 must be equal to the backward stress τ_0, so that $\tau_1 = n\tau$. Thus, the leading stress at the head of the pile up is magnified to n times the applied stress. Given that dislocations are being continuously emitted via cross slip, the stress of the leading dislocation has reached a value higher than the strength of the boundary therefore penetrating it. Dislocations penetrate the grain boundaries leading to dislocations from nearby packets to interact with each other. This interaction leads to the formation of "bumps" on the grain boundaries as can be seen in **Fig 22**. However, it must be noted that since the packet and block boundaries which are high angle grain boundaries are supposed to be impenetrable, the value of the frictional stresses used to model the GBs must be increased in order to obtain more accurate results. Of note as well, is that this microstructural feature has no effect on the mechanical response of the material.

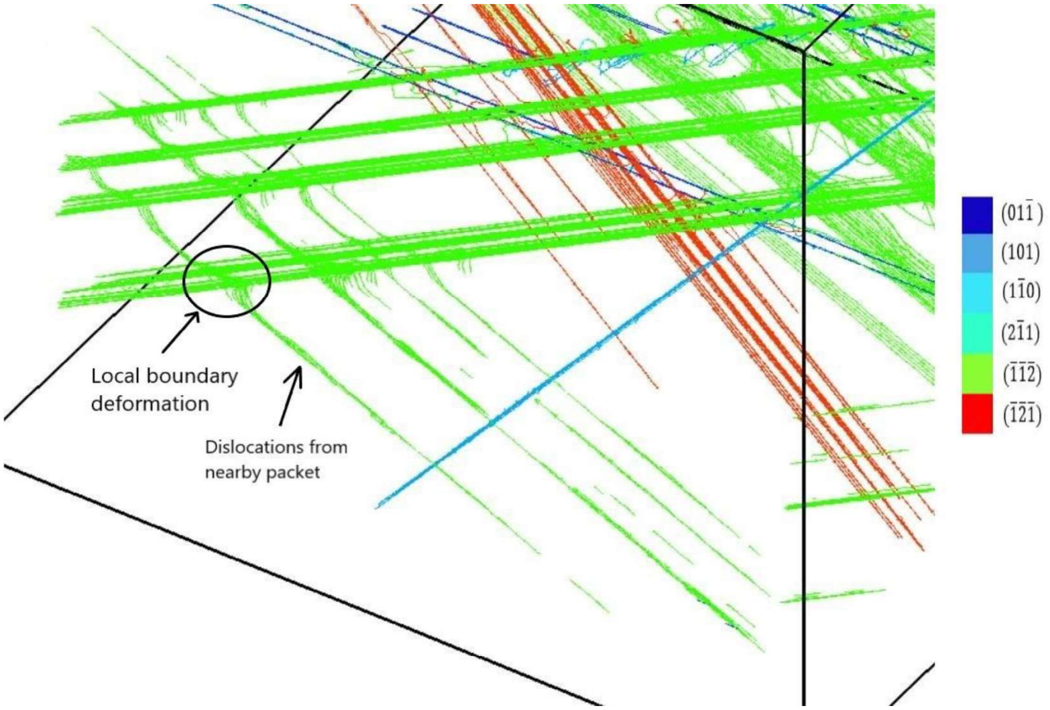

Figure 22. Dislocations from nearby packet interact with dislocations inside RVE due to periodic boundary conditions. Dislocations penetrate the packet boundary at specific locations where the interaction with dislocations from the nearby packet leads to local deformation of the packet boundary.

C. Size effect

The strength of lath martensitic steel was analyzed as a function of the block and packet size are considered as the effective grain size as is seen in **Fig. 23** By examining the flow stresses and plotting those values as a function of $1/\sqrt{d_{packet}}$ and $1/\sqrt{d_{block}}$ where d_{packet} and d_{block} are the packet and block sizes respectively. It is seen that the flow stress is directly proportional to $1/\sqrt{d}$ via a linear equation of the form $\sigma_{flow}(\varepsilon) = \sigma_0 + k(\varepsilon)d^{-0.5}$ indicating that a Hall – Petch type relation exists for the material when the packet or block sizes are considered as the effective grain size.

One must note however, that depending on the manufacturing process of lath martensitic steels, the packet size may increase up to hundreds of microns while the block size reaches only 10 µm. Therefore, the block size should be chosen as the main parameter for size effect investigations.

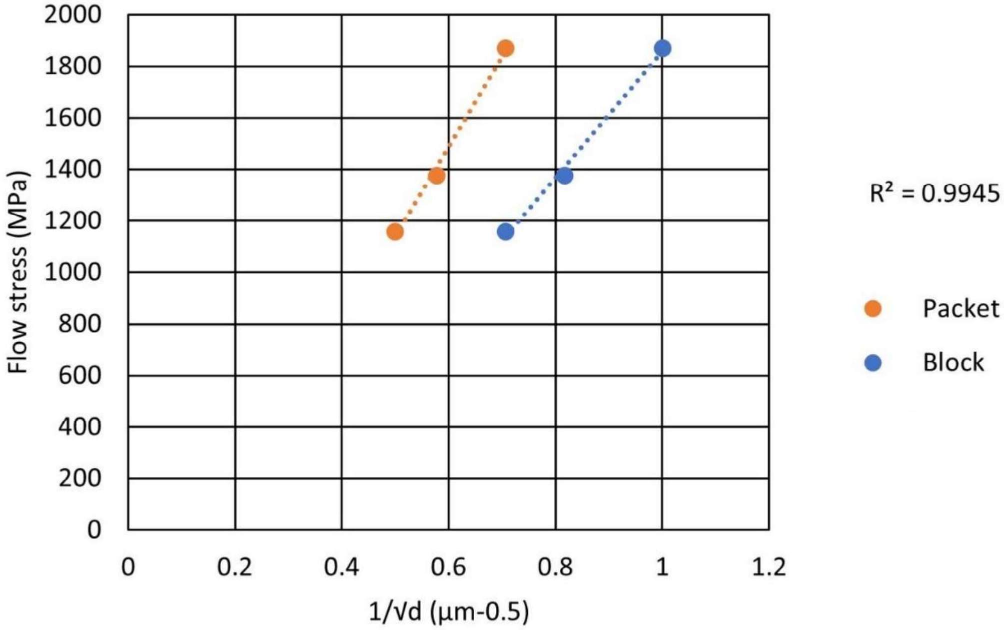

Figure 23. Size effect in lath martensitic steel.

D. Effect of initial dislocation density on the mechanical response

The initial dislocation density depends strongly on the heat treatment and thermomechanical processing with values ranging from 10^{12} to 10^{14} m^{-2} for different thermal processing conditions. For computational purposes, the initial dislocation density used in this hovers around 10^{11} m^{-2}. To examine the effect of different initial dislocation densities on the mechanical response, three scenarios are devised for this purpose. Three different dislocation densities ranging from 2×10^{11} m^{-2} to 10^{12} m^{-2} are used to examine whether or not the initial dislocation density has any effect on the mechanical response. **Table 7** summarizes the three scenarios used.

Table 7. Different initial dislocation densities for the three considered scenarios.

Scenario 1	**Scenario 2**	**Scenario 3**
$\boldsymbol{\rho_{disl} = 2 \times 10^{11}\ m^{-2}}$	$\rho_{disl} = 7 \times 10^{11}\ m^{-2}$	$\rho_{disl} = 10^{12}\ m^{-2}$
1 FR source	2 FR sources	3 FR sources
$\boldsymbol{0.3\ \mu m \leq L_{FR}}$	$0.3\ \mu m \leq L_{FR} \leq 0.35\ \mu m$	$0.3\ \mu m \leq L_{FR} \leq 0.35\ \mu m$
Periodic boundary	Periodic boundary conditions	Periodic boundary conditions

Increasing the initial dislocation density had no noticeable effect on the microstructure evolution and the main microstructural features that arise during plastic deformation (Pile – up, cross slip, etc.). **Fig. 24a** shows the stress – strain curves for different initial dislocation densities. It may be seen that the yield point varies between the three scenarios due to the variability in length of the FR sources between all three simulations. Plastic behavior is fairly similar in all three cases where hardening is balanced by relaxation via cross slip. **Fig. 24b** depicts the dislocation density evolution over time. All three curves follows the same S shaped trend. The 7×10^{11} and 10^{12} m^{-2} scenarios exhibit a higher final dislocation density following yielding due to those two cases having two and three initial FR sources, therefore resulting in more dislocations being emanated from the FR sources which then pile up at the boundaries. Pile ups are cause an increase in dislocation density. The increased number of piled up dislocations leads to more dislocations undergoing cross slip therefore an additional increase in dislocation density and higher final dislocation densities than the 2×10^{11} m^{-2}.

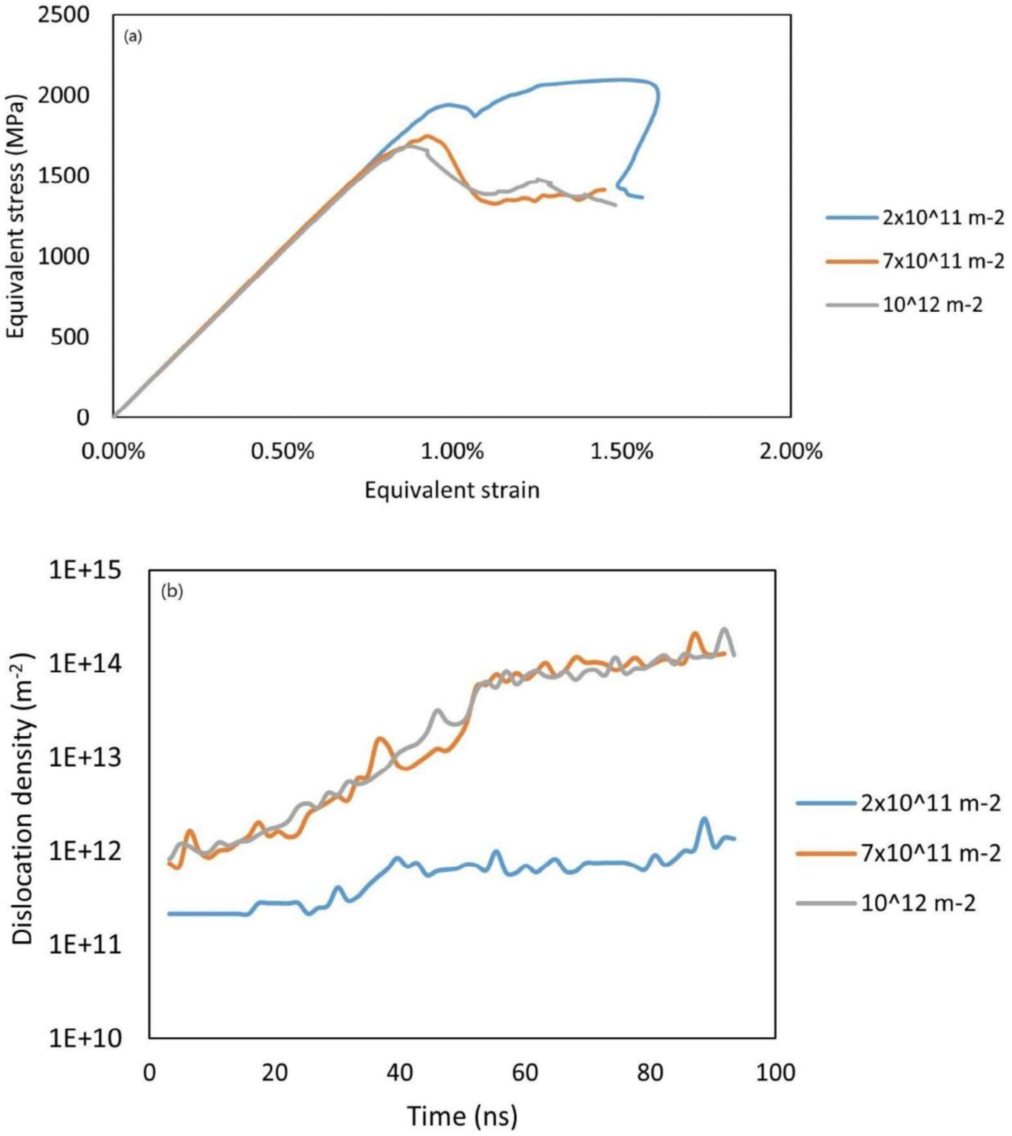

Figure 24. (a) Stress strain curves for different initial dislocation densities. (b) Dislocation density evolution over time for the three different initial dislocation density cases.

E. Precipitate effect on the mechanical response

$M_{23}C_6$ carbides are believed to be the most important precipitates in P91 martensitic steel and are located on the lath boundaries. Due to the importance of precipitates, the role they play on the mechanical response of the material merits an investigation. The precipitate diameter used is $D_p = 200$ nm, and the precipitate spacing $L_p = 571$ nm which is a mean value used based on the findings of D. F. Li et al., 2014b. Lath boundaries are ignored since they have no effect on material flow as demonstrated in Chapter IV. Precipitates are placed where lath boundaries ought to be since $M_{23}C_6$ carbides are located on lath boundaries, as shown in **Fig. 25** which depicts the simulation setup for the precipitate investigation. Precipitates are implemented in MDDP as "frictional spheres" similarly to the way grain boundaries were implemented in MDDP. A 2 μm packet divided into two 1 μm blocks, namely, the V1 and V2 variants used in the simulations above. The sample is subjected to uniaxial tension and the boundary conditions are the same as previous simulations.

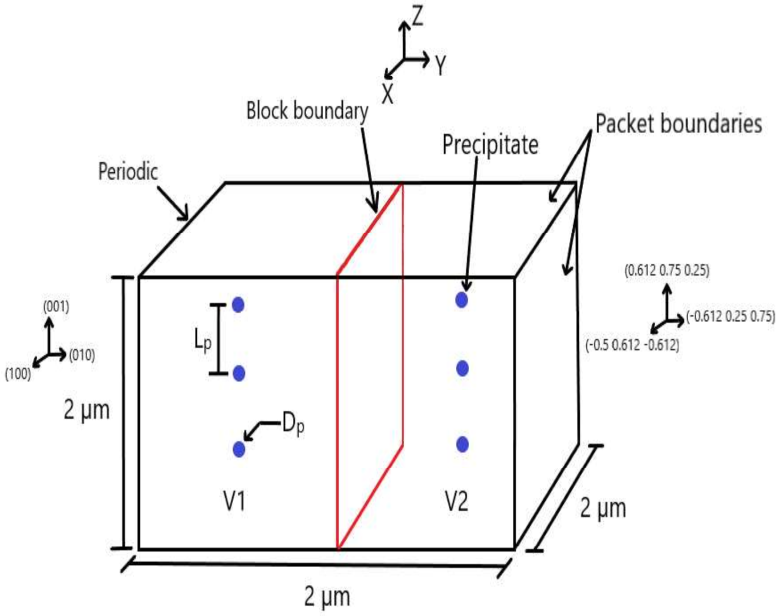

Figure 25. Simulation setup to investigate the effect of precipitates on the mechanical response of the material.

Fig. 26 compares the mechanical response of two 2 μm samples, one with three precipitates with diameter D_p = 200 nm and separated by a distance L_P = 571, and the other sample where precipitates were not considered. The presence of precipitates does not have any noticeable effect on the yield strength of the material. However, the presence of precipitates seems to trigger cross slip at an earlier stage in the loading process. That is, due to the presence of precipitates, cross slip happens earlier than it would have in the case where there is no precipitates.

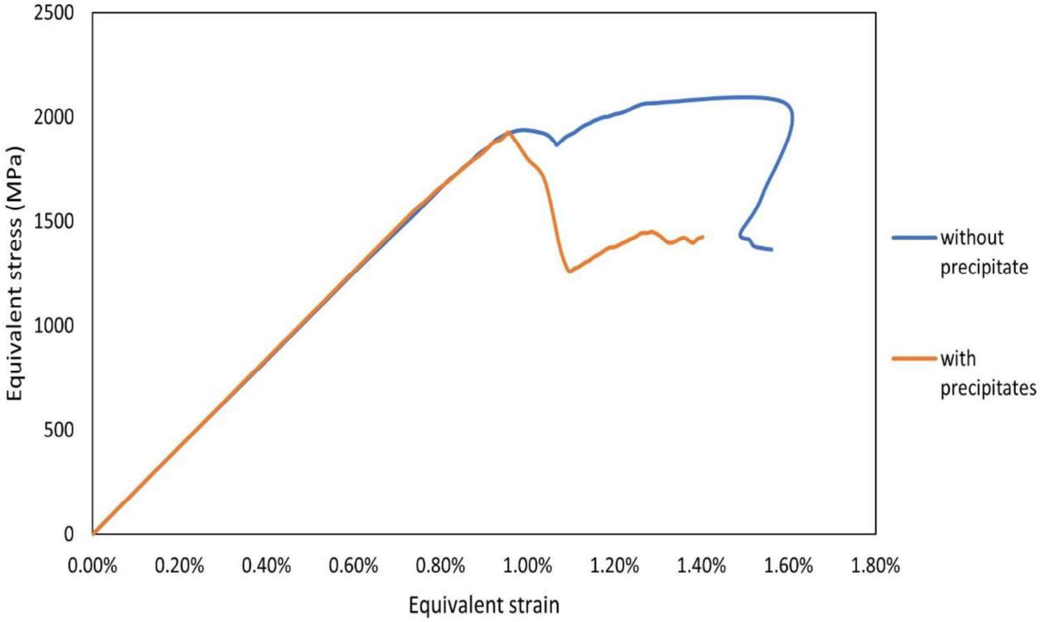

Figure 26. Stress strain diagram for two scenarios, one with precipitates (orange) and one without precipitates (blue).

To further investigate the effect precipitates have on the mechanical response of the material, the microstructural evolution of the material must be studied. Precipitates in crystals tend to bow out dislocations and to be surrounded by dislocation loops after being bypassed by dislocations. Thus, the interaction between precipitates and dislocations, specifically, in the regions close to the precipitates. This is made clear by observing **Fig. 27** which depicts the final microstructural configuration of the material. By observing the material microstructure, it is seen that dislocation loops have formed around precipitates. This indicates that during the deformation process, dislocations have bowed around the precipitates to form a spherical pile up. This mechanism is in accordance with the Orowan mechanism. The effect that precipitates have on the material is made clear by examining the dislocation density evolution of the two considered scenarios. The presence of precipitates in the material act as an obstacle to dislocation motion as discussed above. Precipitates tend to bow dislocations around them and cause a spherical pile up which is evidenced by an increase in dislocation density that is sharper than the case with no precipitates. This sharp increase in dislocation density, as observed in **Fig. 28,** in the case with precipitates occurs at approximately 30 ns into the deformation while the increase in dislocation density occurs at around 50 ns into the loading process for the case without precipitates. The sudden increase in dislocation density is evidence of the cross slip occurring within the material. In order to fully understand the role that precipitates play in material strengthening, further simulations are required where different precipitate spacings L_p and precipitate diameters D_p are used.

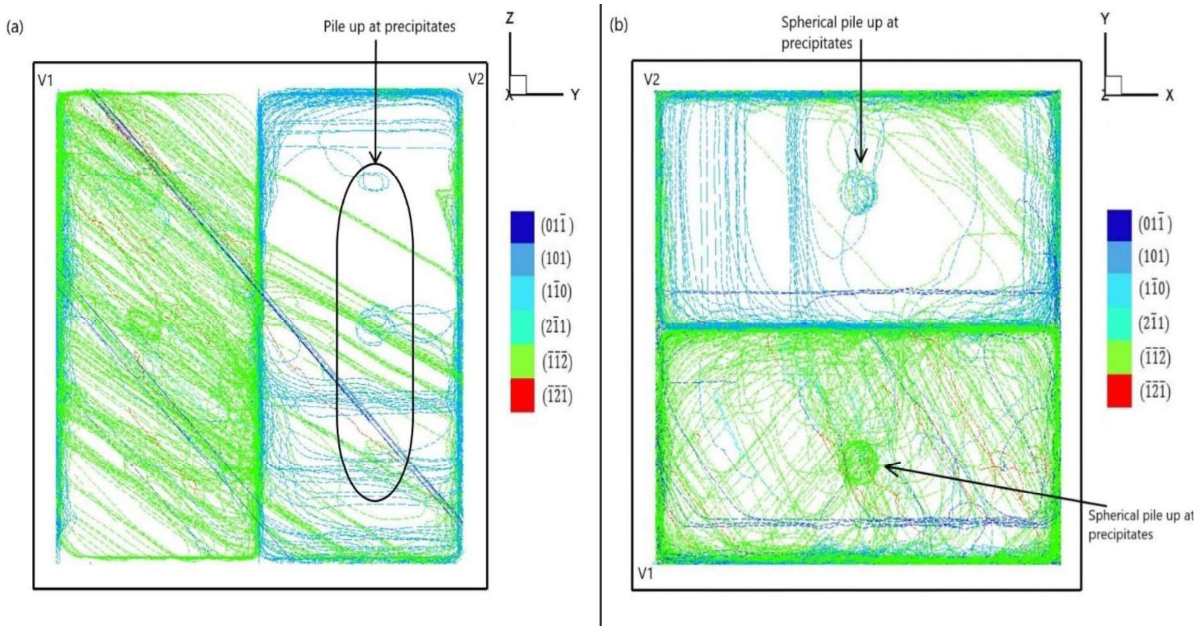

Figure 27. Snapshots of the material microstructure depicting the pile at regions near the precipitates from (a) the front view and (b) the top view

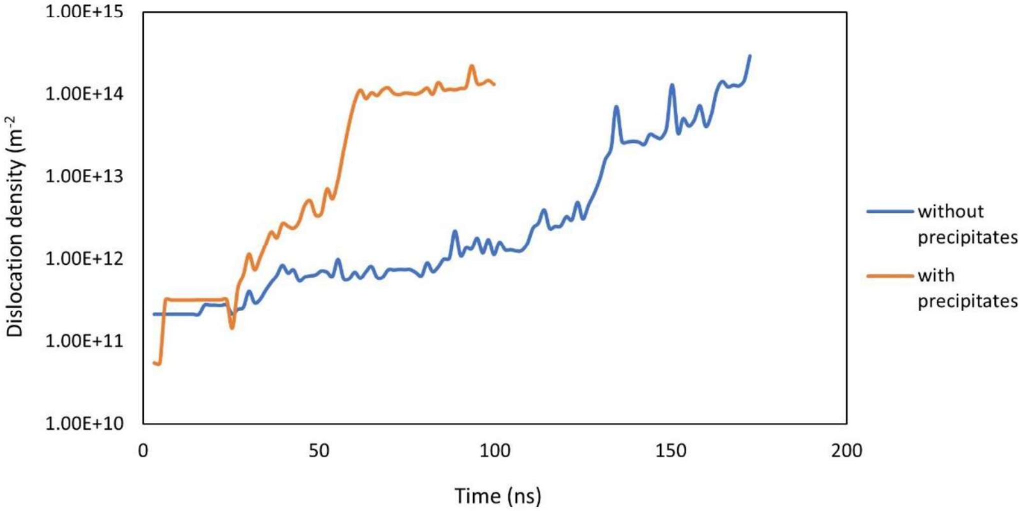

Figure 28. Comparison of the evolution of the dislocation density over time between the case without precipitates (blue) and the case with precipitates (orange).

F. Summary

The K – S orientation relationship governing the crystallographic orientations of martensite blocks has been implemented and the microstructural processes of lath martensitic steel were investigated from a DDD perspective and related to the overall mechanical response of the material.

The deformation mechanisms of lath martensitic steel is mainly dominated by glide. Dislocations pile up against grain boundaries resulting in hardening in the samples. However, the hardening effect is mitigated by a relaxation process in the form of cross slip indicating that cross slip plays a minor role in the mechanical response of the material. The effective grain size for the material should be considered as either the packet or block sizes. However, depending on the manufacturing process, the block size is recommended to be considered the main parameter for any size effect studies.

The effect of precipitates on material flow was also scrutinized and identified from a DDD perspective. It was found that precipitates play an important role in retarding dislocation motion throughout the material by bowing dislocations around them and causing a pile up. Dislocations tend to pile up around precipitates and in regions around them, leading to material hardening and an increase in dislocation density.

CHAPTER VI

CONCLUSIONS AND FUTURE DIRECTIONS

The microstructure of martensitic steels was modelled by first implementing lath boundaries and studying their effect on the mechanical response of the material. Dislocation interactions with the lath boundaries were examined and it was observed that dislocations undergo a pin – unpin mechanism at the lath boundaries which results in local plastic deformation in the form of bumps at the location where dislocation were unpinned. The lath width was considered for being an effective grain size and it was concluded that it should not be taken as an effective grain size for martensitic steels since lath boundaries have a negligible effect on material flow. Packet and block boundaries were implemented through the use of a frictional barrier to represent these high angle grain boundaries. The K – S orientation relationship was also incorporated in MDDP to accurately study the interactions between 2 different blocks inside a packet by simulating three packet sizes. The dominant mechanisms for plastic deformation were found to be crystallographic slip including glide and cross slip which occurs along 45° bands in the [100] direction and along 30° bands in the [010] direction. Packet – packet interactions were also reported where packet boundaries undergo local plastic deformation in the form of bumps on the boundaries where dislocations are able to penetrate into the nearby packets. Block size was found to be the effective grain size in martensitic steels. The initial dislocation density was found to have no effect on the material response. Precipitates were implemented and their effect on the mechanical response was evaluated determined using MDDP. Precipitates play a crucial role in retarding dislocation motion leading to an increase in dislocation density. However, the size of the precipitates and the precipitate spacing may play a significant role in shaping the material response to an applied load which shall be investigated in future works. Further study is needed to model a polycrystalline material with more than just two blocks using dislocation dynamics.

REFERENCES

Atkinson, M. (1984). Strain Hardening Behavior of Polycrystalline Iron and Low-Carbon Steels - a Statistical Analysis. *Metallurgical Transactions. A, Physical Metallurgy and Materials Science*, *15 A*(6), 1185–1192. https://doi.org/10.1007/bf02644713

Barrett, R. A., O'Donoghue, P. E., & Leen, S. B. (2014). A dislocation-based model for high temperature cyclic viscoplasticity of 9-12Cr steels. *Computational Materials Science*, *92*, 286–297. https://doi.org/10.1016/j.commatsci.2014.05.034

Callister, W. D. (1991). Materials science and engineering: An introduction (2nd edition). *Materials & Design*, *12*(1), 59. https://doi.org/10.1016/0261-3069(91)90101-9

Dewald, M., & Curtin, W. A. (2011). Multiscale modeling of dislocation/grain-boundary interactions: III. 60° dislocations impinging on Σ3, Σ9 and Σ11 tilt boundaries in Al. *Modelling and Simulation in Materials Science and Engineering*, *19*(5). https://doi.org/10.1088/0965-0393/19/5/055002

Dewald, M. P., & Curtin, W. A. (2007a). Multiscale modelling of dislocation/grain-boundary interactions: I. Edge dislocations impinging on Σ11 (1 1 3) tilt boundary in Al. *Modelling and Simulation in Materials Science and Engineering*, *15*(1). https://doi.org/10.1088/0965-0393/15/1/S16

Dewald, M. P., & Curtin, W. A. (2007b). Multiscale modelling of dislocation/grain boundary interactions. II. Screw dislocations impinging on tilt boundaries in Al. *Philosophical Magazine*, *87*(30), 4615–4641. https://doi.org/10.1080/14786430701297590

Dundulis, G., Janulionis, R., Grybėnas, A., Makarevičius, V., & Dundulis, R. (2017). Numerical and experimental investigation of low cycle fatigue behaviour in P91 steel. *Engineering Failure Analysis*, *79*(February), 285–295. https://doi.org/10.1016/j.engfailanal.2017.05.001

Furuhara, T., Kikumoto, K., Saito, H., Sekine, T., Ogawa, T., Morito, S., & Maki, T. (2008). Phase transformation from fine-grained austenite. *ISIJ International*, *48*(8), 1038–1045. https://doi.org/10.2355/isijinternational.48.1038

Ghassemi-Armaki, H., Maaß, R., Bhat, S. P., Sriram, S., Greer, J. R., & Kumar, K. S. (2014). Deformation response of ferrite and martensite in a dual-phase steel. *Acta Materialia*, *62*(1), 197–211. https://doi.org/10.1016/j.actamat.2013.10.001

Golański, G., & Mroziński, S. (2013). Low cycle fatigue and cyclic softening behaviour of martensitic cast steel. *Engineering Failure Analysis*, *35*, 692–702. https://doi.org/10.1016/j.engfailanal.2013.06.019

Golden, B. J., Li, D. F., O'Dowd, N. P., & Tiernan, P. (2014). Microstructural modeling of P91 martensitic steel under uniaxial loading conditions. *Journal of Pressure Vessel Technology, Transactions of the ASME*, *136*(2), 1–6. https://doi.org/10.1115/1.4026028

Golden, Brian J., Li, D. F., Guo, Y., Tiernan, P., Leen, S. B., & O'Dowd, N. P. (2016). Microscale deformation of a tempered martensite ferritic steel: Modelling and experimental study of grain and sub-grain interactions. *Journal of the Mechanics and Physics of Solids*, *86*, 42–52. https://doi.org/10.1016/j.jmps.2015.09.015

Hansen, N. (2005). Boundary strengthening in undeformed and deformed polycrystals. *Materials Science and Engineering A*, *409*(1–2), 39–45.

https://doi.org/10.1016/j.msea.2005.04.061

Jo, K. R., Seo, E. J., Hand Sulistiyo, D., Kim, J. K., Kim, S. W., & De Cooman, B. C. (2017). On the plasticity mechanisms of lath martensitic steel. *Materials Science and Engineering A*, *704*(August), 252–261. https://doi.org/10.1016/j.msea.2017.08.024

Kitahara, H., Ueji, R., Tsuji, N., & Minamino, Y. (2006). Crystallographic features of lath martensite in low-carbon steel. *Acta Materialia*, *54*(5), 1279–1288. https://doi.org/10.1016/j.actamat.2005.11.001

Kitahara, H., Ueji, R., Ueda, M., Tsuji, N., & Minamino, Y. (2005). Crystallographic analysis of plate martensite in Fe-28.5 at.% Ni by FE-SEM/EBSD. *Materials Characterization*, *54*(4–5), 378–386. https://doi.org/10.1016/j.matchar.2004.12.015

Kondo, S., Mitsuma, T., Shibata, N., & Ikuhara, Y. (2016). Direct observation of individual dislocation interaction processes with grain boundaries. *Science Advances*, *2*(11), 1–7. https://doi.org/10.1126/sciadv.1501926

Kurdjumow, G., & Sachs, G. (1930). Der Mechanismus der Stahlhärtung. *Die Naturwissenschaften*, *18*(22), 534. https://doi.org/10.1007/BF01513427

Li, D. F., Barrett, R. A., O'Donoghue, P. E., O'Dowd, N. P., & Leen, S. B. (2017). A multi-scale crystal plasticity model for cyclic plasticity and low-cycle fatigue in a precipitate-strengthened steel at elevated temperature. *Journal of the Mechanics and Physics of Solids*, *101*, 44–62. https://doi.org/10.1016/j.jmps.2016.12.010

Li, D. F., Golden, B. J., & O'Dowd, N. P. (2014a). Multiscale modelling of mechanical response in a martensitic steel: A micromechanical and length-scale-dependent framework for precipitate hardening. *Acta Materialia*, *80*, 445–456. https://doi.org/10.1016/j.actamat.2014.08.012

Li, D. F., Golden, B. J., & O'Dowd, N. P. (2014b). Multiscale modelling of mechanical response in a martensitic steel: A micromechanical and length-scale-dependent framework for precipitate hardening. *Acta Materialia*, *80*, 445–456. https://doi.org/10.1016/j.actamat.2014.08.012

Li, S., Zhu, G., & Kang, Y. (2016). Effect of substructure on mechanical properties and fracture behavior of lath martensite in 0.1C-1.1Si-1.7Mn steel. *Journal of Alloys and Compounds*, *675*, 104–115. https://doi.org/10.1016/j.jallcom.2016.03.100

Liu, B., Eisenlohr, P., Roters, F., & Raabe, D. (2012). Simulation of dislocation penetration through a general low-angle grain boundary. *Acta Materialia*, *60*(13–14), 5380–5390. https://doi.org/10.1016/j.actamat.2012.05.002

Liu, B., Raabe, D., Eisenlohr, P., Roters, F., Arsenlis, A., & Hommes, G. (2011). Dislocation interactions and low-angle grain boundary strengthening. *Acta Materialia*, *59*(19), 7125–7134. https://doi.org/10.1016/j.actamat.2011.07.067

Luo, H., Wang, X., Liu, Z., & Yang, Z. (2020). Influence of refined hierarchical martensitic microstructures on yield strength and impact toughness of ultra-high strength stainless steel. *Journal of Materials Science and Technology*, *51*, 130–136. https://doi.org/10.1016/j.jmst.2020.04.001

MAKI, T., TSUZAKI, K., & TAMURA, I. (1980). The Morphology of Microstructure Composed of Lath Martensites in Steels. *Transactions of the Iron and Steel Institute of Japan*, *20*(4), 207–214. https://doi.org/10.2355/isijinternational1966.20.207

Meade, E. D., Sun, F., Tiernan, P., & O'Dowd, N. P. (2018). Experimental study and multiscale modelling of the high temperature deformation of tempered martensite under multiaxial loading. *Materials Science and Engineering A*, *737*(July), 383–392. https://doi.org/10.1016/j.msea.2018.09.040

Michiuchi, M., Nambu, S., Ishimoto, Y., Inoue, J., & Koseki, T. (2009). Relationship between local deformation behavior and crystallographic features of as-quenched lath martensite during uniaxial tensile deformation. *Acta Materialia*, *57*(18), 5283–5291. https://doi.org/10.1016/j.actamat.2009.06.021

Morito, S., Tanaka, H., Konishi, R., Furuhara, T., & Maki, T. (2003). The morphology and crystallography of lath martensite in Fe-C alloys. *Acta Materialia*, *51*(6), 1789–1799. https://doi.org/10.1016/S1359-6454(02)00577-3

Morito, S., Yoshida, H., Maki, T., & Huang, X. (2006). Effect of block size on the strength of lath martensite in low carbon steels. *Materials Science and Engineering A*, *438–440*(SPEC. ISS.), 237–240. https://doi.org/10.1016/j.msea.2005.12.048

Morsdorf, L., Jeannin, O., Barbier, D., Mitsuhara, M., Raabe, D., & Tasan, C. C. (2016). Multiple mechanisms of lath martensite plasticity. *Acta Materialia*, *121*, 202–214. https://doi.org/10.1016/j.actamat.2016.09.006

Na, H., Nambu, S., Ojima, M., Inoue, J., & Koseki, T. (2014). Crystallographic and microstructural studies of lath martensitic steel during tensile deformation. *Metallurgical and Materials Transactions A: Physical Metallurgy and Materials Science*, *45*(11), 5029–5043. https://doi.org/10.1007/s11661-014-2461-4

Nagesha, A., Valsan, M., Kannan, R., Bhanu Sankara Rao, K., & Mannan, S. L. (2002). Influence of temperature on the low cycle fatigue behaviour of a modified 9Cr-1Mo ferritic steel. *International Journal of Fatigue*, *24*(12), 1285–1293. https://doi.org/10.1016/S0142-1123(02)00035-X

Nambu, S., Michiuchi, M., Ishimoto, Y., Asakura, K., Inoue, J., & Koseki, T. (2009). Transition in deformation behavior of martensitic steel during large deformation under uniaxial tensile loading. *Scripta Materialia*, *60*(4), 221–224. https://doi.org/10.1016/j.scriptamat.2008.10.007

Ohmura, T., Minor, A. M., Stach, E. A., & Morris, J. W. (2004). Dislocation-grain boundary interactions in martensitic steel observed through in situ nanoindentation in a transmission electron microscope. *Journal of Materials Research*, *19*(12), 3626–3632. https://doi.org/10.1557/JMR.2004.0474

Pandey, C., Giri, A., & Mahapatra, M. M. (2016). Effect of normalizing temperature on microstructural stability and mechanical properties of creep strength enhanced ferritic P91 steel. *Materials Science and Engineering A*, *657*, 173–184. https://doi.org/10.1016/j.msea.2016.01.066

Patriarca, L., Abuzaid, W., Sehitoglu, H., & Maier, H. J. (2013). Slip transmission in bcc FeCr polycrystal. *Materials Science and Engineering A*, *588*, 308–317. https://doi.org/10.1016/j.msea.2013.08.050

Pelleg, J. (2013). Mechanical properties of materials. In *Solid Mechanics and its Applications* (Vol. 190). https://doi.org/10.1007/978-94-007-4342-7

Protocol, U. T. H. E. K., & Union, T. H. E. E. (1990). Power & Energy Magazine. *Power*, *february*, 65–74.

R.Viswanathan. (1989). Damage Mechanisms and Life Assessment of High Temperature Components. In *Materials Ageing and Component Life Extension* (Issue L). http://books.google.com/books?hl=en&lr=&id=psNWNNXB02EC&oi=fnd&pg=PA1&dq=Damage+Mechanisms+and+Life+Assestment+of+High-Temperature+Components&ots=0SHl0tVPPg&sig=58pNsVPbBU1AgX50jncRTt

1V-xE

Roters, F., Diehl, M., Shanthraj, P., Eisenlohr, P., Reuber, C., Wong, S. L., Maiti, T., Ebrahimi, A., Hochrainer, T., Fabritius, H. O., Nikolov, S., Friák, M., Fujita, N., Grilli, N., Janssens, K. G. F., Jia, N., Kok, P. J. J., Ma, D., Meier, F., … Raabe, D. (2019). DAMASK – The Düsseldorf Advanced Material Simulation Kit for modeling multi-physics crystal plasticity, thermal, and damage phenomena from the single crystal up to the component scale. *Computational Materials Science*, *158*(April 2018), 420–478. https://doi.org/10.1016/j.commatsci.2018.04.030

Sauzay, M., Brillet, H., Monnet, I., Mottot, M., Barcelo, F., Fournier, B., & Pineau, A. (2005). Cyclically induced softening due to low-angle boundary annihilation in a martensitic steel. *Materials Science and Engineering A*, *400–401*(1-2 SUPPL.), 241–244. https://doi.org/10.1016/j.msea.2005.02.092

Shamsujjoha, M. (2020). Evolution of microstructures, dislocation density and arrangement during deformation of low carbon lath martensitic steels. *Materials Science and Engineering A*, *776*(October 2019). https://doi.org/10.1016/j.msea.2020.139039

Shen, Z., Wagoner, R. H., & Clark, W. A. T. (1988). Dislocation and grain boundary interactions in metals. *Acta Metallurgica*, *36*(12), 3231–3242. https://doi.org/10.1016/0001-6160(88)90058-2

Shibata, A., Nagoshi, T., Sone, M., Morito, S., & Higo, Y. (2010). Evaluation of the block boundary and sub-block boundary strengths of ferrous lath martensite using a micro-bending test. *Materials Science and Engineering A*, *527*(29–30), 7538–7544. https://doi.org/10.1016/j.msea.2010.08.026

Shin, S. E., Nambu, S., Kim, H., Inoue, J., Koseki, T., & Lee, S. J. (2020). Evaluation of factors influencing the lath martensitic deformation behavior of multi-layered steels. *Materials Science and Engineering A*, *785*(April). https://doi.org/10.1016/j.msea.2020.139353

Sun, F., Meade, E. D., & O'Dowd, N. P. (2019). Strain gradient crystal plasticity modelling of size effects in a hierarchical martensitic steel using the Voronoi tessellation method. *International Journal of Plasticity*, *119*(March), 215–229. https://doi.org/10.1016/j.ijplas.2019.03.009

Sun, F., Meade, E. D., & O′Dowd, N. P. (2018). Microscale modelling of the deformation of a martensitic steel using the Voronoi tessellation method. *Journal of the Mechanics and Physics of Solids*, *113*, 35–55. https://doi.org/10.1016/j.jmps.2018.01.009

Sutton, A. P., Balluffi, R. W., Lüth, H., & Gibson, J. M. (1996). Interfaces in Crystalline Materials and Surfaces and Interfaces of Solid Materials . *Physics Today*, *49*(9), 88–88. https://doi.org/10.1063/1.2807772

Wang, L., Li, M., & Almer, J. (2014). Investigation of deformation and microstructural evolution in Grade 91 ferritic-martensitic steel by in situ high-energy X-rays. *Acta Materialia*, *62*(1), 239–249. https://doi.org/10.1016/j.actamat.2013.10.003

Zbib, H. M., & Diaz de la Rubia, T. (2002). A multiscale model of plasticity. *International Journal of Plasticity*, *18*(9), 1133–1163. https://doi.org/10.1016/S0749-6419(01)00044-4

Zinkle, S. J., & Busby, J. T. (2009). Structural materials for fission & fusion energy. *Materials Today*, *12*(11), 12–19. https://doi.org/10.1016/S1369-7021(09)70294-9